

ABSTRACT

Mapping the Distribution of Methane Hydrate Beneath Woolsey Mound, Mississippi Canyon Block 118, Gulf of Mexico

Alan R. Gunnell, M.S.

Mentor: John A. Dunbar, Ph.D.

An active methane vent (Woolsey Mound) in Mississippi Canyon Block 118 (MC118), Gulf of Mexico, has been a focus of persistent research. This vent area contains both active and dormant vents and blocks of methane hydrate outcropping on the seafloor. In light of the large amount of collaborative work done by the Gulf of Mexico-Hydrate Research Consortium (GOM-HRC), surface characteristics and mound chemistry is understood, but the distribution of hydrate within the HSZ is unknown.

High-frequency seismic imaging of the mound is hindered by the presence of free gas, hydrate, and biogenic carbonate blocks at the water bottom. By performing seismic attribute analyses on the high-frequency seismic data previously collected by the GOM-HRC and combining direct current resistivity data, the likely distribution consists of high-saturation methane hydrate in pockets along deep-seeded faults and low-saturation hydrate and disseminated free gas surrounding these faulted areas beneath Woolsey Mound.

Mapping the Distribution of Methane Hydrate Beneath Woolsey Mound, Mississippi
Canyon Block 118, Gulf of Mexico

by

Alan R. Gunnell, B.S.

A Thesis

Department of Geology

Stacy C. Atchley, Ph.D., Chairperson

Submitted to the Graduate Faculty of
Baylor University in Partial Fulfillment of the
Requirements for the Degree
of
Master of Science

Approved by the Thesis Committee

John A. Dunbar, Ph.D., Chairperson

Robert Jay Pulliam, Ph.D.

Gregory A. Benesh, Ph.D.

Accepted by the Graduate School
December 2013

J. Larry Lyon, Ph.D., Dean

Copyright © 2013 by Alan R. Gunnell

All right reserved

TABLE OF CONTENTS

1) Table of Contents	iv
2) List of Figures	v
3) List of Tables	vii
4) Acknowledgements	viii
5) Dedication	ix
6) Chapter One: Introduction	1
a. Methane Hydrate	1
7) Chapter Two: Previous Work	12
a. Seismic Data	12
i. Reflection Seismic Method	12
ii. Shallow Source – Deep Receiver Seismic Method	17
iii. High Resolution Seismic and Core Data	21
b. Resistivity Data	22
i. Direct Current Resistivity Method	22
ii. System Configuration and Acquisition	25
iii. Results of the DCR Survey	30
8) Chapter Three: Methods	32
a. Seismic Attribute Analysis	32
b. Combination of DCR with SSDR data	34
9) Chapter Four: Results	37
a. Seismic Results	37
b. SSDR Line 27	40
c. SSDR Line 18	47
10) Chapter Five: Discussion	52
11) Chapter Six: Conclusions	54
12) References	55

LIST OF FIGURES

Figure 1: Distribution of methane hydrate across the world	2
Figure 2: Conditions for the natural occurrence of methane hydrate	3
Figure 3: Expansion rate of methane hydrate as a result of dissociation	5
Figure 4: In-place reserves of methane hydrate	6
Figure 5: Push core of churned up marine mud and methane hydrate fragments	7
Figure 6: Location of Woolsey Mound in the Gulf of Mexico	9
Figure 7: Bathymetric view of Woolsey Mound	10
Figure 8: Acoustic impedance versus percentage of hydrocarbon saturation	13
Figure 9: Origin of a bottom simulating reflector	14
Figure 10: Cartoon of the shallow-source deep-receiver method	17
Figure 11: AUV-borne chirp sub-bottom profile and SDR 3D grid	19
Figure 12: High-scatter zone beneath Woolsey Mound	20
Figure 13: Gradient array schematic	22
Figure 14: In situ hydrate concentration	24
Figure 15: ROV and converted SuperSting™ DCR system	25
Figure 16: Cartoon of the DCR array	26
Figure 17: Overlay of SDR 3D grid with DCR Lines	27
Figure 18: DCR Line 1 extending over Woolsey Mound	30
Figure 19: DCR Line 2 extending over Woolsey Mound	30
Figure 20: Different seismic attribute profiles of a representative inline	32
Figure 21: SDR survey lines overlain by DCR Lines 1 and 2	35
Figure 22: A SDR inline across the active vent on Woolsey Mound	37
Figure 23: SDR Line 27 amplitude seismic attribute profile	38
Figure 24: SDR Line 27 instantaneous phase seismic attribute profile	39

Figure 25: SDR Line 27 amplitude envelope seismic attribute profile	40
Figure 26: SDR Line 27 Hilbert seismic attribute profile	41
Figure 27: SDR Line 27 amplitude inversion seismic attribute profile	42
Figure 28: Interpretation of SDR Line 27	43
Figure 29: Interpretation of SDR Line 27	46
Figure 30: Mapped extents of likely and potential methane hydrate	47

LIST OF TABLES

Table 1: Significant dates of methane gas hydrate history	1
Table 2: Amounts of organic carbon sources worldwide	4

ACKNOWLEDGEMENTS

This research was made possible from two grants from the Department of Energy. The first was awarded to John Dunbar DE-PS26-06NT42820-00 and made it possible to build the Direct Current Resistivity Instrument and array used on this seafloor experiment. The second award was given to the Gulf of Mexico-Hydrate Research Consortium (GOM-HRC), DOE Award Number DE-FC26-02NT41628, which supplied us with ship time and manpower used to deploy the instrument and conduct the survey. GOM-HRC also provided access to the SSSR seismic data used in the study. Seismic Micro Technology, ASIA PTE, Ltd. provided the software used to interpret the SSSR data. Advanced Geosciences, Inc. provided help with hardware and software modifications needed to collect and process resistivity data on the deep seafloor. Specialty Devices, Inc. help by interfacing the resistivity instrument with the power and control features of the remotely operated vehicle used in the study. SDI was also instrumental in coordinating the shipboard operations for the duration of the over 30 hours of acquisition time.

Of course, this would also not have been possible without the help, patience, and guidance of John Dunbar and Baylor University.

DEDICATION

To all those people in my life who love and support me:

To

my wife Minda, my kids, Samuel, Jacob, Nathan, and Heidi,
this is for you.

Your patience, love and support enabled me
to continue to work to get it completed

and

To my parents, Val and Jane
and parents-in-law, Brad and Cathy

who have also been great supports to my family and I during this time.

CHAPTER ONE

Introduction

Methane Hydrate

Methane hydrate is an ice-like compound composed of crystal lattice cages of hydrogen-bonded water molecules, with at most one methane molecule in each cage (Sloan, 1998). People have been aware of methane hydrate for over 100 years (Table 1), while the distribution of methane hydrate throughout the world has become more of a recent topic of study, especially with the increased consideration of it as a potential energy resource (Demirbas, 2010; Figure 1).

Table 1: Significant dates of methane gas hydrate history taken from Demirbas, 2010.

Milestones of methane gas hydrates	
Year	Progress
1888	Methane gas hydrate first measured by Villard
1934	Hydrates discovered to plug gas pipelines
1952	si crystal unit confirmed
1964	Hydrates found in Siberian permafrost
1970	Oceanographers drill through methane gas hydrate deposit
1981	Drilling vessel in Guatemala recovers a methane hydrate sample intact
1992	Beginning for intentionally looking for methane gas hydrate deposits

Natural occurrences of methane hydrate form under pressure and temperature regimes, termed the hydrate stability zone (HSZ), in the sediments along continental shelves and in permafrost regions throughout the world (Figure 2A and 2B).

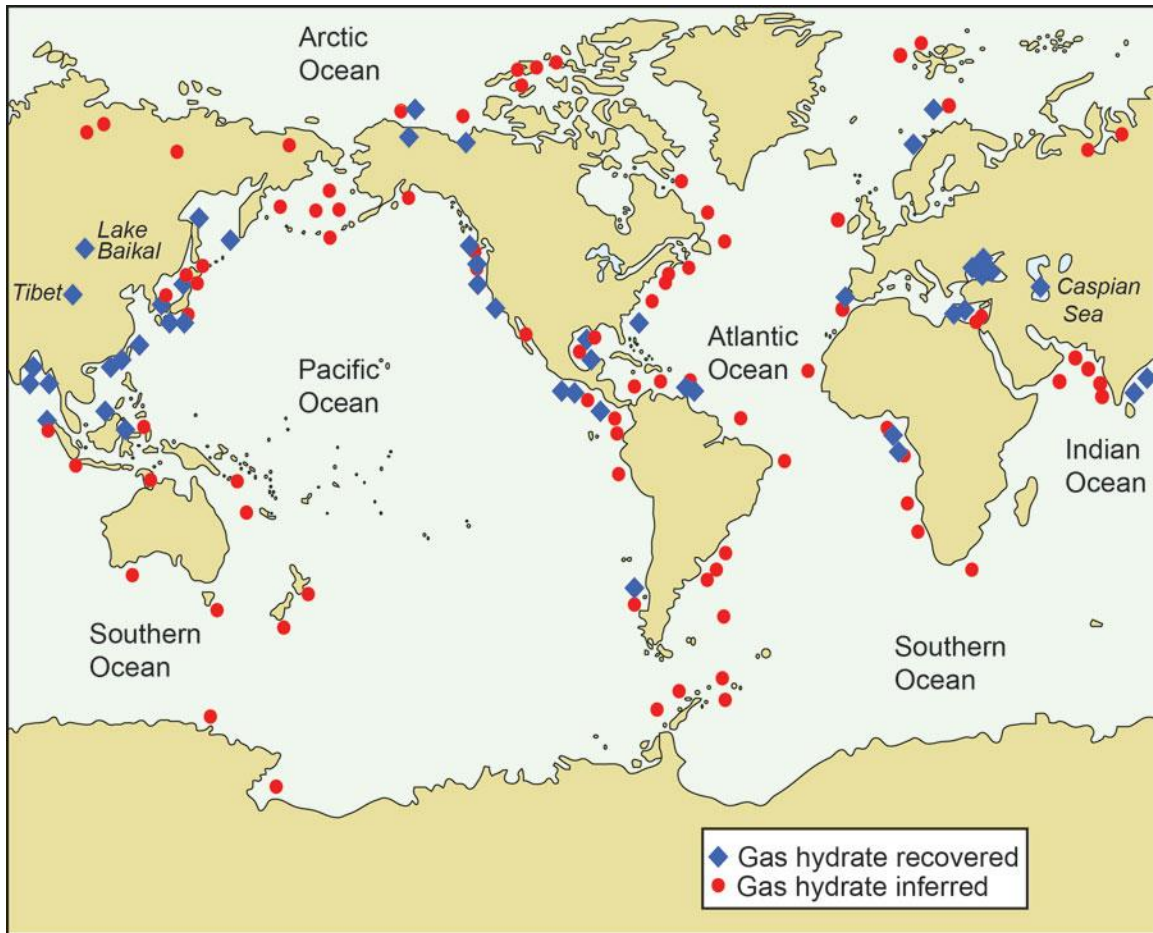


Figure 1: Distribution of methane hydrate across the world. Figure posted by Ruppel, C., and Noserale, D., 2012 USGS.

Worldwide estimates of the amounts of organic carbon sources indicate that the largest resource of untapped organic carbon is methane hydrate. Demirbas (2010) estimated the total amount of gas hydrates to be ten thousand to eleven thousand gigatons of organic carbon reserves (Table 2).

Kvenvolden (1993) estimated that the total amount of methane hydrate in all geologic settings is equivalent to a 40-m-thick blanket covering the entire surface of Earth. An estimated 700,000 trillion ft^3 (TCF) of methane may be contained in these deposits, which is equivalent to a minimum two times that of all other forms of hydrocarbon discovered to date (Demirbas, 2010).

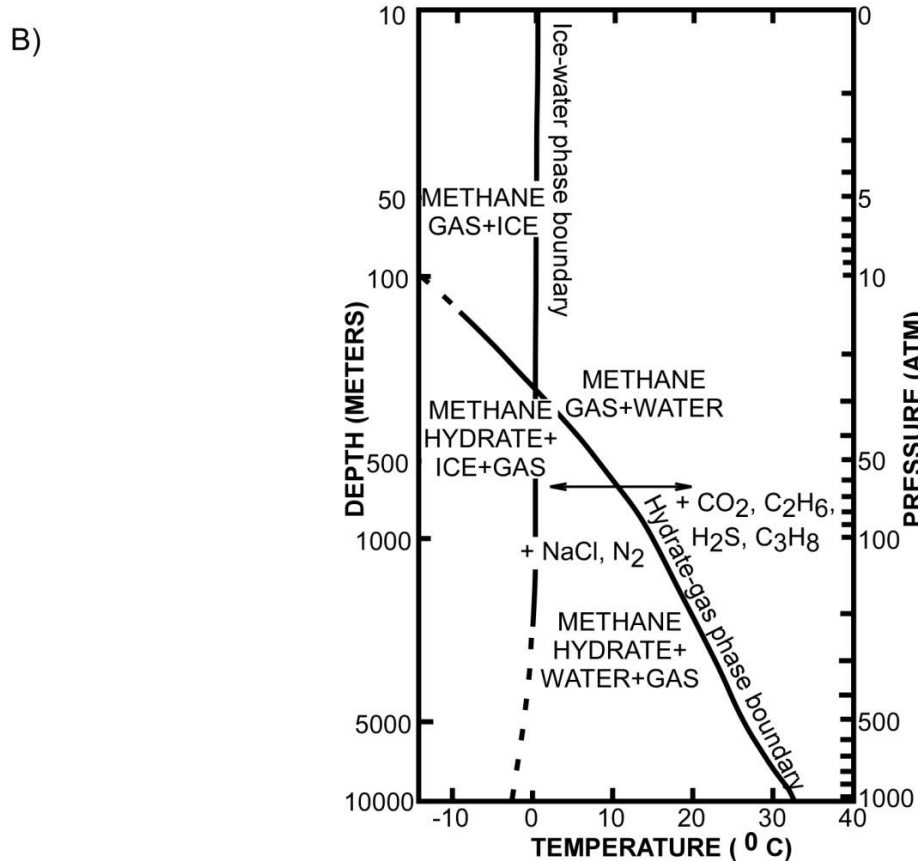
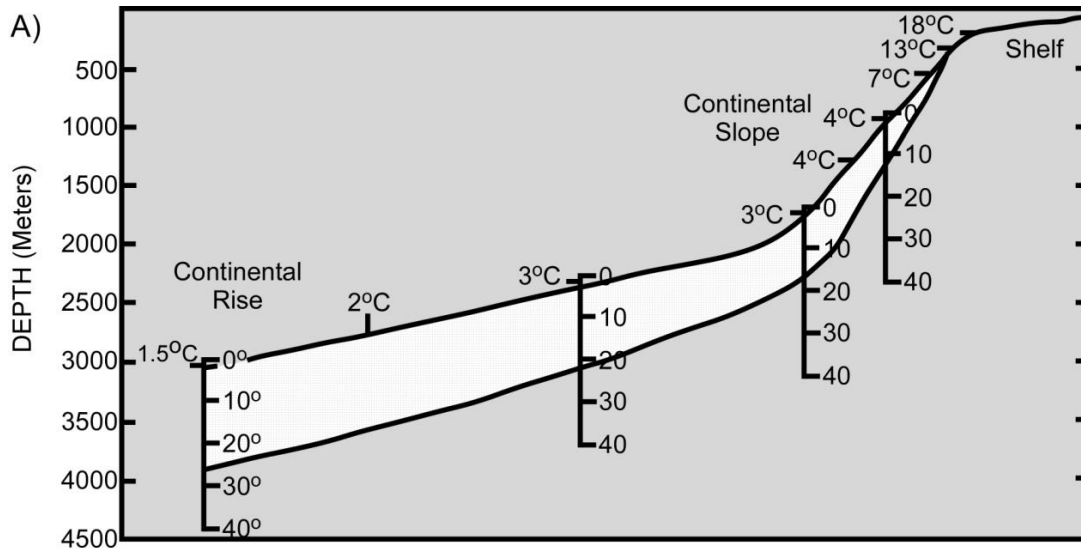


Figure 2: Conditions for the natural occurrence of methane hydrate. A) Figure from Kvenvolden and McMenamin (1980) showing the rapid temperature increase as one travels up the continental slope. The gas hydrate zone is in white. The location of this study is along the continental slope and is subject to lower temperatures. B) This phase diagram modified from Kvenvolden and McMenamin (1980) and Collett (1983) shows the dynamic nature of the formation of methane hydrate and the different forms that methane can take depending on pressure, temperature, and depth.

Table 2: Amounts of organic carbon sources worldwide. Table originally from Demirbas, 2010, identifies the great potential for the use of methane hydrate as an alternate fuel source for the future. With the abundance of methane hydrate, the potential for an influx of methane into the atmosphere if there is an increase of the earth's temperature. If the temperature of the world's oceans were to increase then slope stability will also decrease and simultaneously release methane into the atmosphere and with the amount of methane available it would be a major issue for living things.

Worldwide amounts of organic carbon sources	
Source of organic carbon	Amount (Gigaton)
Gas hydrates (onshore and offshore)	10,000 - 11,000
Recoverable and non-recoverable fossil fuels (oil, coal, gas)	5000
Soils	1400
Dissolved organic matter	980
Land biota	880
Peat	500
Others	70

This vast, untapped storehouse of hydrocarbon is of interest as an alternate energy resource for the near future (Demirbas, 2010) and as a potentially important player in global warming. The fear is that warming in polar regions and rising seawater temperatures will cause dissociation of methane hydrate in permafrost regions and along continental shelves. As the disassociation of methane hydrate occurs, a cubic unit of methane hydrate will expand to 164 times its original size in the form of gas and some excess water (Kvenvolden 1993, Figure 3). If this happens, the escaping gas will be introduced into the atmosphere, greatly increasing the greenhouse effect (Dickens et al., 1997). Another issue associated with methane hydrate has to do with the weakening of the continental slopes where hydrates are found. As the hydrate disassociates, resulting sub-sea landslides can potentially cause problems for oil and gas infrastructure.

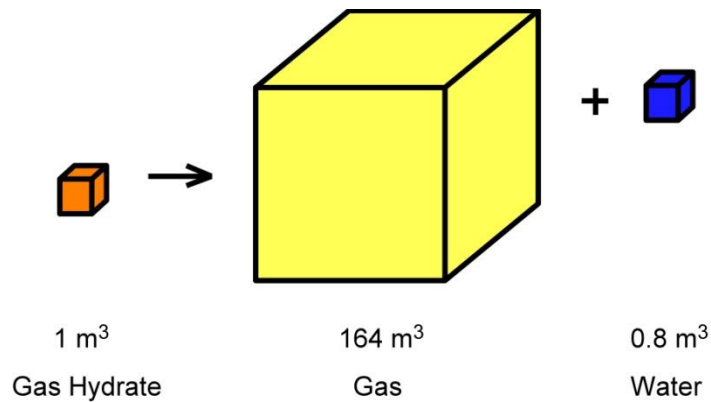


Figure 3: Expansion of methane hydrate as a result of dissociation. This figure is modified from Kvenvolden, 1993. This cartoon illustrates the expansion rate of a cubic unit of methane hydrate as either pressure is released or the temperature increases. A cubic unit will expand to 164 times its original size in the form of gas with a small amount of water excess.

Exploitation of methane hydrate as an energy resource will require adaptation of existing exploration and production methods used in conventional petroleum operations, and possibly the development of entirely new methods, specifically tailored to the hydrate problem. Hydrate deposits with characteristics similar to those of conventional petroleum deposits will require less adaptation and development of new technology and hence will likely be the first to be exploited. The so-called hydrate resource pyramid, subdivides the world's hydrate deposits based the host sedimentary environments in which the hydrate occurs (Figure 4 from Boswell, 2009, *Science*, v. 325, p. 957).

The largest segment, at the base of the pyramid, accounts for over 80% of all hydrate. Hydrates in this segment occur in low concentrations within undeformed marine muds. Recovery of methane from these deposits will require extensive development of new technology, which means that it will be many decades before hydrates in this segment could be practically exploited, if at all.

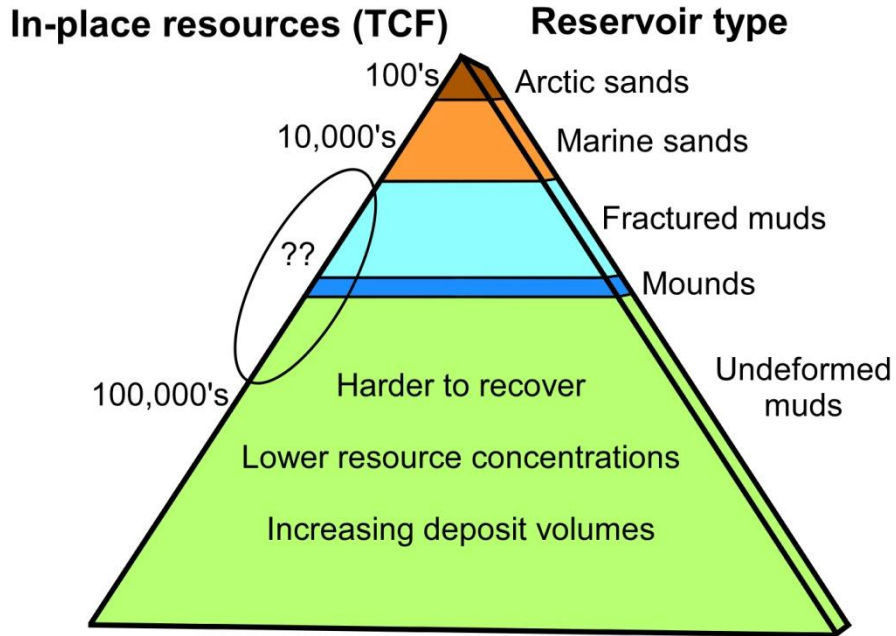


Figure 4: The in-place reserves of methane hydrate with respect to the sediments types in which they are found. This figure is modified from Boswell, 2009. Little is known about the amount of methane hydrate found in fractured muds and mounds.

The smallest segment of hydrate deposits, at the top of the pyramid, corresponds to hydrates contained within the pores of sand reservoirs. This segment accounts for only 10,000 TCF (5%) of the total World's total hydrate deposits. Joint industry and governmental drilling and exploration projects have recently evaluated sand layers containing laterally continuous, thick accumulations of methane hydrate using adaptations of conventional coring and seismic methods (Rose et al, 2009; Boswell et al., 2009). In particular, rock-physics-based approaches to interpretation of reflections from discrete hydrate-bearing sand intervals have been reliable for predicting hydrate saturation in this setting (Sain et al., 2010; Ghosh et al. 2010).

Between these two segments, in the middle of the pyramid, are hydrates that occur in fractured marine muds and hydrate mounds (Figure 5).

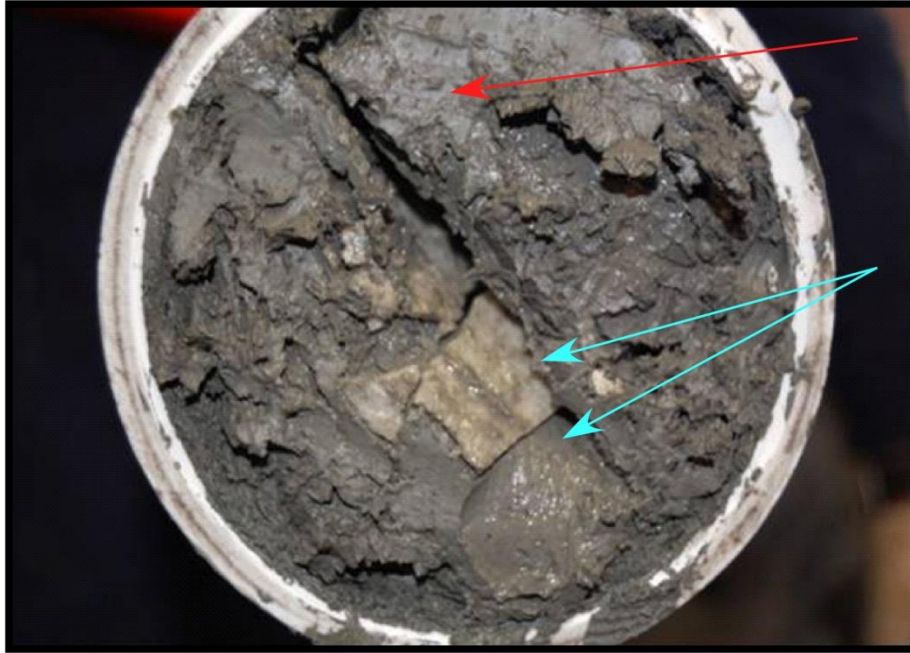


Figure 5: This is a core sample taken from Woolsey Mound of methane hydrate chunks surrounded by organic-rich mud. Figure reprinted from *Marine and Petroleum Geology*, Vol. 44, Simonetti et al., Spatial distribution of gas hydrates from high-resolution seismic and core data, Woolsey Mound, Northern Gulf of Mexico, pp. 21-33, 2013 with permission from Elsevier. The blue arrows point to fragments of methane hydrate. The red arrow points to the organic muds surrounding the methane hydrate. The core diameter is 6 inches.

Hydrate mounds on the seafloor occur where thermogenic methane from petroleum source rocks migrates up from great depth along faults and into the HSZ near the seafloor. The future potential as an energy resource is high because this segment accounts for more than twice as much methane as the sand reservoir segment (12%). The hydrates in this environment mainly occur as fracture-fill in shallow sediments in deep marine settings. Francisca et al. (2005) observed that in those areas where methane hydrate was found in cores, they were predominantly in vertical fractures. Because these highly disrupted sediments do not produce coherent seismic reflections, exotic methods such as seismic tomography and full waveform seismic inversion have been proposed to map hydrate deposits in fracture muds and hydrate mounds (Thakur et al., 2007).

Seafloor mining has been proposed as a possible production method (Beggs et al., 2008). In spite of these initial efforts, much work remains to develop practical exploration and production methods for hydrates in this segment.

Seafloor mounds, such as Woolsey Mound, in Mississippi Canyon, Block 118, Gulf of Mexico (MC118), are a common geologic setting for the occurrence of methane hydrate within deformed fine-grained sediments. The Gulf of Mexico-Hydrate Research Consortium (GOM-HRC) has actively studied Woolsey Mound for more than 10 years (Figure 6). GOM-HRC is a group of academic institutions and various State and Federal agencies formed to conduct multi-disciplinary studies of hydrate systems in the northern Gulf of Mexico.

The GOM-HRC has explored the Woolsey mound by manned submersible dives, extensive shallow coring within the mound area, and multi-beam profiling of the mound topography (DOE, 2006). This work has established that there are both active and dormant methane vents at the site and that gas hydrate is exposed at the seafloor in the active vents (Figure 7). Recent work by Simonetti et al. (2013) integrated jumbo piston cores with high-resolution seismic reflection data to provide a subsurface distribution of gas hydrates.

Hato et al. (2006) recognized that the likely goal of future hydrate exploration will be to find areas of high hydrate saturation. Hence, it may not be necessary to quantify hydrate saturation through its complete range. Instead, their strategy is to identify intervals of high hydrate saturation in stratigraphic test wells by looking for intervals with both elevated P-wave velocity and electrical resistivity on well logs.

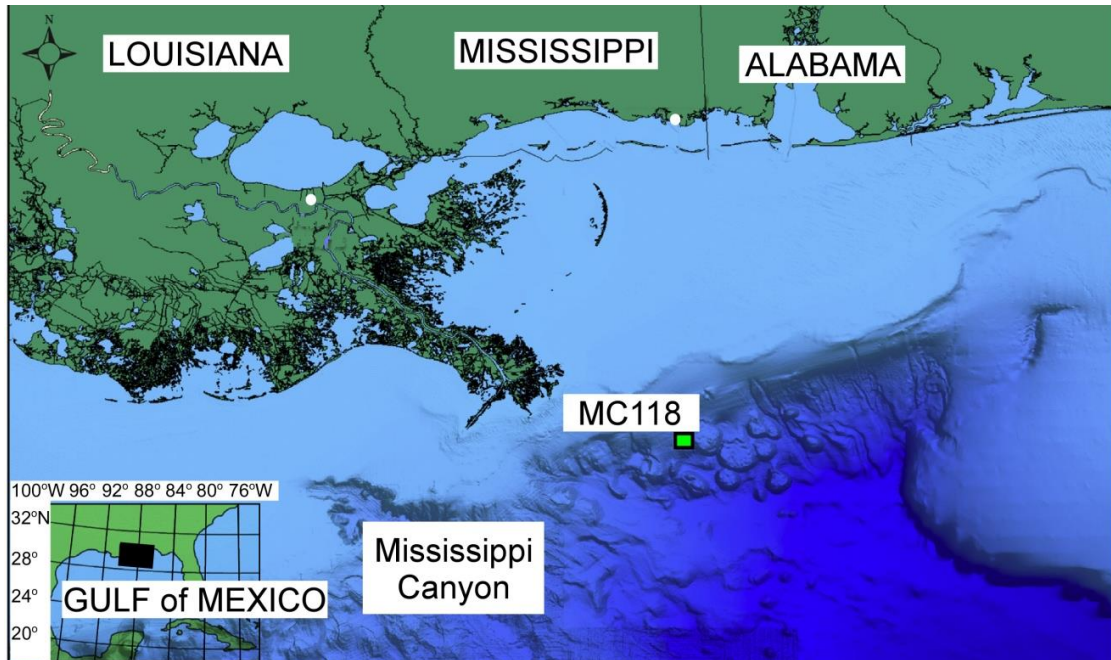


Figure 6: This is the location of Woolsey Mound in MC118, GOM. It is approximately 60 miles southeast of Louisiana and the hydrate mound in this study sits just on the edge of the continental shelf in the region. This location is the shallowest expression of a methane hydrate mound in the GOM. This has made it an interesting and useful location for further study. Data is originally from NOAA; Simonetti et al., 2013.

Once the intervals of interest are identified, a range of seismic attributes from the high saturation intervals on co-located seismic data are compared to the seismic attributes from other, non-hydrate bearing intervals. Seismic attributes are quantitative properties of the seismic data, such as amplitude, phase, frequency, energy, attenuation rate, etc., that may be qualitative indicators of sediment properties of interest.

This seismic attribute analysis is replacing the P-wave data. In their study, Hato et al. (2006) found that intervals of high hydrate saturation correlated with areas of high seismic attenuation rate. They then mapped areas of high seismic attenuation rate throughout a 3D seismic volume as a proxy for areas of high hydrate saturation.

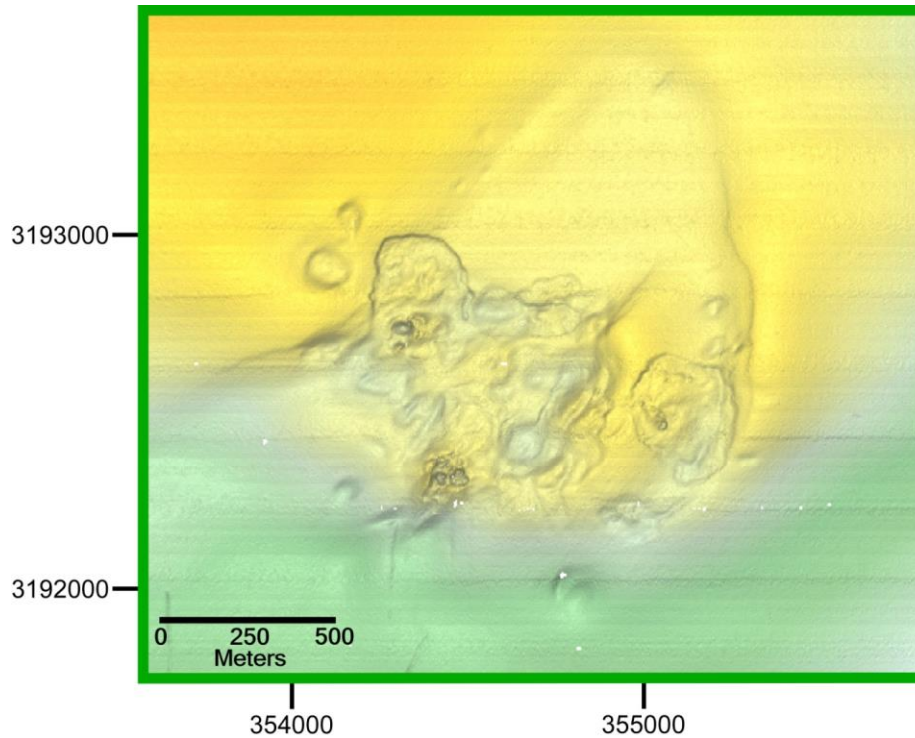


Figure 7: Bathymetric view of Woolsey mound taken from McGee et al. 2009. There are a number of vents within the mound. Those to the east are no longer active, whereas those to the west are active. Geographic coordinates are UTM Zone 16, meters, Easting and Northing.

In this study I test an approach similar to the one used by Simonetti et al. (2013) for mapping the distribution of areas of high hydrate saturation an active methane hydrate mound (Wolsey Mound), in Mississippi Canyon Block 118, Gulf of Mexico. The approach I take to identify the distribution of methane hydrate beneath Woolsey mound is to combine seismic attribute analysis and direct current resistivity and use the correlations to infer zones of high accumulations of methane hydrate and zones of disseminated hydrate.

CHAPTER TWO

Previous Work

Seismic Data

Reflection Seismic Method

Since the 1930s, the seismic reflection method has been the principle geophysical tool used in petroleum exploration. In the seismic reflection method, a mechanical or explosive source is used to produce seismic pulses at regular intervals along a profile. The pulses travel into the subsurface, reflect from stratigraphic interfaces, and return to the surface where they are recorded by an array of seismic sensors. These data are then processed to produce images of the stratal geometry. Modern methods for acquiring marine seismic reflection data for petroleum exploration, involving airgun source arrays and towed hydrophone receiver arrays, evolved from methods used for academic study of the seafloor starting in the 1950s. Today the marine seismic reflection method is a mature technology, with existing 3D data sets covering the entire Northern Gulf of Mexico available on a subscription basis. Because of its extensive use and the wide availability of existing data, the seismic reflection method has naturally been the first choice for the location and characterization of methane hydrate.

Detecting methane hydrate using reflection seismology relies on the contrast in the velocities with which seismic waves travel through rock and sediment with water, free gas, and hydrate in the pore spaces. Compressional or so called P-waves travel through an elastic medium at a velocity given by

$$V_p = \sqrt{\frac{K + \frac{4}{3}\mu}{\rho}}, \quad (1)$$

where K is the bulk modulus, μ is the shear modulus, and ρ is the density of the medium. The bulk modulus is the resistance of a medium to volume change, whereas the shear modulus is the resistance to shape distortion without volume change.

In poorly consolidated sediments with fluid or gas filling the pores, the shear modulus depends on the friction between grains and is small relative to the bulk modulus. The bulk modulus of the sediment as a whole is in part controlled by the framework of grains and in part by the nature of the pore-filling material. A small amount of free gas in the pores does not significantly change the overall density of the sediment, but drastically reduces the overall bulk modulus. Hence, replacing pore water with free gas dramatically reduces the seismic velocity of sediment. This effect increases with increasing gas saturation, but much of the velocity reduction occurs for only 10 to 20 % gas saturation. In contrast, the bulk modulus of hydrate is 50% higher than that of liquid water (3.3×10^9 Pa versus 2.2×10^9 Pa) and its shear modulus is 7.9×10^9 Pa (Helgerud et al. 1999). As a result, P velocity increases with increasing hydrate saturation (Hesthammer et al. 2010, Figure 8).

However, theoretical models predict that the amount of the increase for a given level of hydrate saturation is sensitive to whether the hydrate is simply pore-filling, without grain contact, grain supporting, or grain cementing (Helgerud et al., 1999). This sensitivity is borne out by laboratory experiments on sands, which show a 30% increase in P-wave velocity from 0 to 40% saturation of pore-filling hydrate and an 80% increase in velocity for 40% saturation of partially cementing hydrate (Priest et al. 2009).

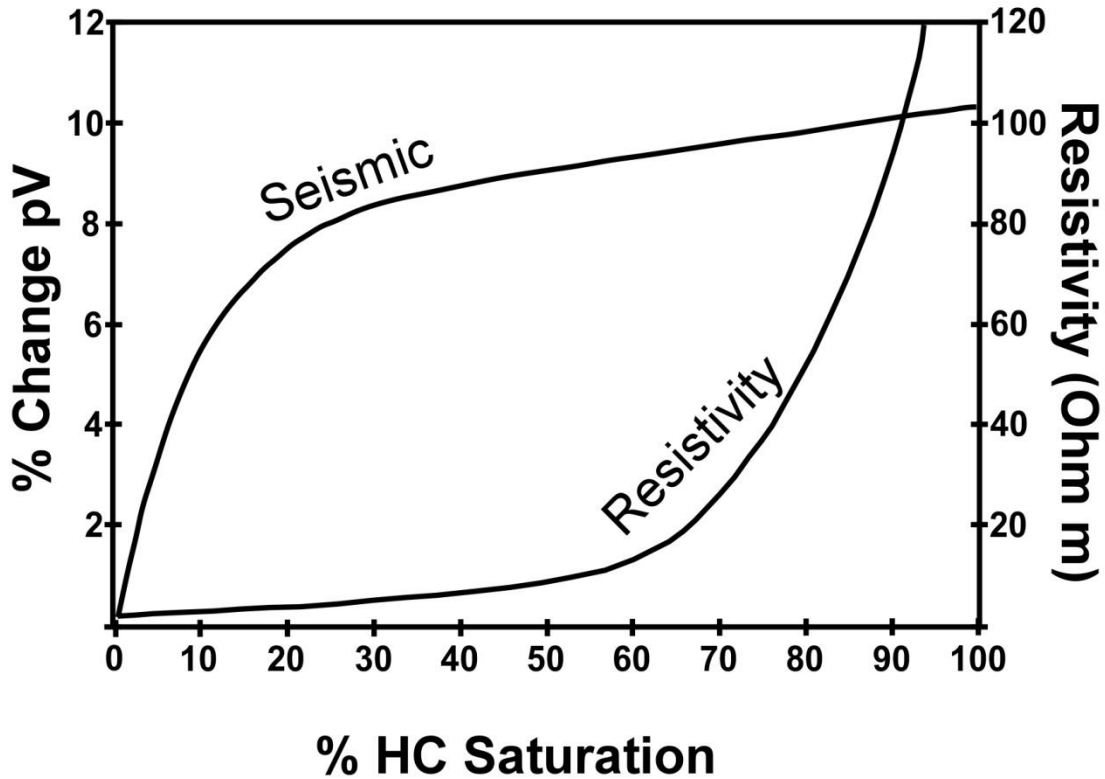


Figure 8: Relationship of acoustic impedance versus hydrocarbon saturation. This figure is modified from Hesthammer et al., 2010. This figure shows the relationship of acoustic impedance versus the percentage change in hydrocarbon saturation.

These laboratory results show that the level of hydrate saturation within sediment cannot be uniquely determined from seismic reflection data alone and that natural hydrate may exhibit different seismic signatures, depending on the environment in which it forms (Priest, et al., 2009). The problem is that areas of low saturations of cementing hydrate would be indistinguishable from areas of high saturations of pore-filling hydrate.

In spite of these limitations, several approaches have been proposed for estimating hydrate saturation from seismic reflection data. The most direct approach is to analyze the amplitudes of reflections from interfaces between hydrate-bearing and non-hydrate-bearing sediment. The amplitude of a reflection of a normal incident seismic wave from

an interface between media of contrasting seismic velocities and densities is proportional to the reflection coefficient (RC) between the two media

$$RC = \frac{\rho_2 v_2 - \rho_1 v_1}{\rho_2 v_2 + \rho_1 v_1}, \quad (2)$$

where ρ_1 and v_1 are the density and seismic velocity of the medium in which the wave is traveling and ρ_2 and v_2 are the velocity and density of the contacting medium.

Bottom simulating reflectors (BSRs) are laterally extensive reflectors that parallel the seafloor and commonly cross reflections from dipping lithologic boundaries (Figure 9).

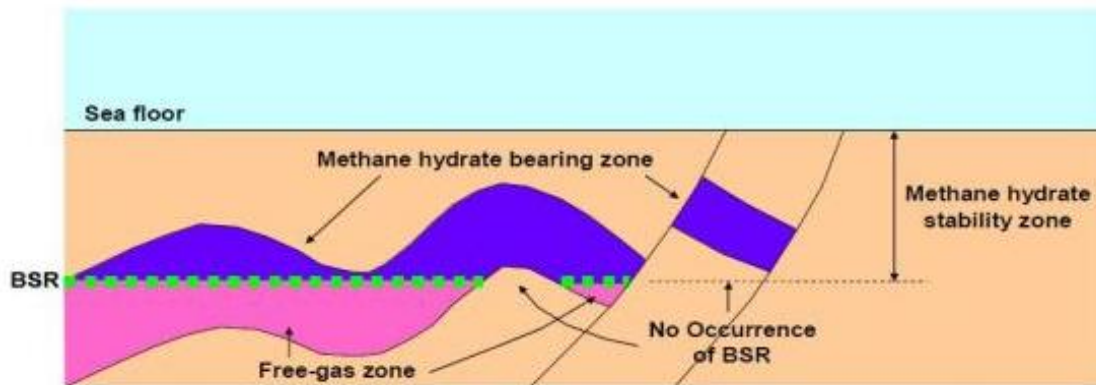


Figure 9: Origin of a bottom simulating reflectors (BSRs). Figure from Saeki et al. (2008). A boundary, the BSR, is the location of gas filled sediment underlying sediments with hydrate (most often methane hydrate). An occurrence of a BSR often is an indication of biogenic processes is supplying the organic material for the formation of hydrate. In this figure there is also a fault indicating the potential for the influence of thermogenic processes. The acoustic signature associated with a BSR is a polarity reversal of reflections returning from the gas filled sediments. This polarity reversal is due to the change in pore fluids and is indirectly attributed to the presence of methane hydrate, which provides the trapping mechanism. The name given to such reflections is a seismic bright spot, because they commonly stand out as high-amplitude reflections.

BSRs are inferred to mark the phase boundary between hydrate-bearing sediment above and free-gas-bearing sediment below the base of the HSZ and are the primary indicator of

marine hydrate deposits (Shipley et al., 1979). The depth to a BSR is determined by the depth at which the local geotherm intersects the HSZ, and hence BSRs tend to parallel the seafloor in deep marine settings (Weitemeyer et al., 2006). Although BSR are reliable indicators of the presence of hydrate, they provide little or no information about the volume or distribution of hydrate within the overlying HSZ.

In cases in which isolated sand layers occur within the HSZ, thermal gas can migrate upward from depth into the sand layers and fill pore spaces with hydrate to varying levels of saturation. In these cases, the strength and character of the reflection between the hydrate-bearing sand and surrounding water-saturated sediment changes with changing hydrate saturation and can be used to estimate the volume of hydrate in place (Cordon et al., 2006). In the absence of such sand intervals, the HSZ can have surprisingly low reflectivity to signals in the exploration seismic band (10 to 80 Hz) (Paull and Matsumoto, 1996). Where internal reflections are absent, reflection amplitude analysis does not provide information about the hydrate distributions within the stability zone.

In cases in which hydrate is believed to be disseminated throughout the HSZ, seismic tomographic inversion is an alternate approach that has been proposed for determining hydrate concentrations (Lodolo et al., 2002). In its most common implementation, seismic tomography is a ray-theory based seismic inversion method in which the subsurface is subdivided into discrete cells, and then an iterative process is used to find the cell velocities for which the forward ray-trace model best predicts the observed travel times between successive reflectors (Böhm et al., 2000). In the absence of reflections from within the HSZ, tomographic inversion can be used to determine the

average velocity from the seafloor reflection to the BSR. Hydrate saturations are then inferred from either theoretical (Gei and Carcione, 2003; Zillmer et al., 2005) or empirical (Priest et al., 2009) velocity - hydrate saturation relationships.

Given the fundamental ambiguity of hydrate saturation estimates based on P wave velocity alone, efforts have been made to incorporate additional forms of seismic data into the estimation process. The strategy is to eliminate or reduce the ambiguity in the relationship between P wave velocities and hydrate saturation by adding other measurements that are also sensitive to hydrate saturation. These efforts include measurement of the change in reflection amplitude versus incidence angle (AVA, Ojha and Sain, 2007) and measurement of both P and S wave velocity, using multi-component seafloor receivers (Hardage et al, 2006; Kumar et al., 2006). Although, these methods have merit, there is currently no widely accepted seismic method for quantifying hydrate saturation.

Shallow-Source Deep-Receiver Seismic Method

Shallow-source deep-receiver (SSDR) data are single-channel seismic data collected using a water-gun source at a shallow depth beneath the water's surface and a single hydrophone receiver towed at mid-water, halfway between the surface and the seafloor. The SSDR method is able to achieve sub-meter resolution while also obtaining hundreds of meters of sub-bottom penetration. McGee et al. (2009) used the SSDR method, with a strong acoustic source (80 in³ water gun) near the surface of the water and a mid-water hydrophone receiver several hundred meters beneath the source (Figure 10).

The seismic data used in this study were acquired by Tom McGee et al. (2005), on an orthogonal grid of 30 east-west oriented lines, nominally spaced 200 m apart and

58 north-south with the lines nominally spaced 100 m apart, centered on Woolsey Mound, within MC118 (Figure 11).

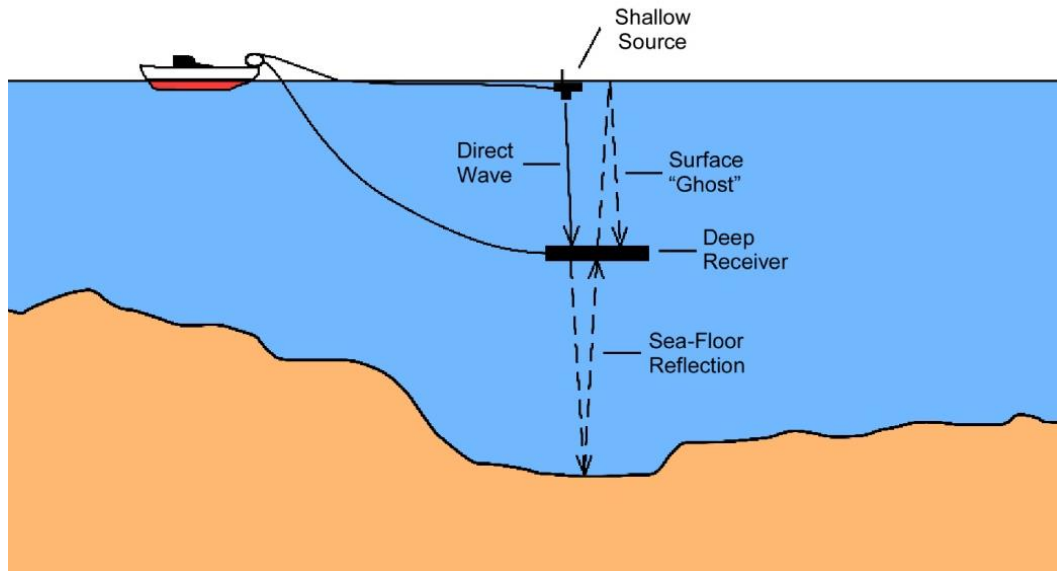


Figure 10: Shallow-source deep-receiver seismic method modified from McGee et al. (2009) showing a deep-water seismic technique for profiling the shallow sub-bottom. The high resolution technique is called surface-source-deep-receiver (SSDR) because it uses a conventional source towed at the surface and a hydrophone receiver towed at deeply directly beneath the source.

At mid-water depths, the receiver is deep enough to record a far-field source signature for each seismic shot and is yet still far enough above the bottom to record the complete source signature without interference from the water bottom reflection (McGee et al., 2009). The signatures are used in post-survey processing to remove the phase of the seismic pulse and shorten the length of the pulse, and thereby improve resolution (McGee et al., 2008). The resulting processed data have meter-scale vertical resolution 500 to 600 meters below the seafloor. The base of the hydrate stability zone (BHSZ) in this area is believed to be at a depth of 200 m below the seafloor (McGee et al., 2008). Seismic reflection profiles indicate enormous amounts of local lateral variability and the

extent of seismically blank zones above a BSR within individual methane hydrate regions (Paull et al., 1996).

A drawback of the SSSDR method is that it results in high levels of low frequency noise caused by cable strumming associated with dragging the long receiver cable through the water column. McGee et al. (2008) used high-pass digital filters applied in post-survey processing to remove the low frequency noise, while preserving seismic signals in the band from 100 to 1000 Hz. The dominant frequency of sub-bottom returns was 200 Hz. For the purposes of this study the same SSSDR data were low-pass filtered and down-sampled to a sample rate of 0.2 milliseconds. Down-sampling was done so that the data could be viewed and interpreted using commercially available seismic interpretation software.

The SSSDR method provides significant information about stratal and fault geometries in the shallow subsurface across nine square kilometers adjacent to the mound. However, directly beneath the mound, scattering of the signal renders the seismic data incoherent (Figure 12).

This zone of incoherent seismic data is likely the result of the combination of pockets of free gas, hydrate, and authigenic carbonate blocks in the shallow subsurface, all with irregular geometries. Variations in the amplitude and character of the scattered returns are apparent. However, attempts to interpret these patterns in terms of the distribution of hydrate within the stability zone are found in Simonetti et al. (2003).

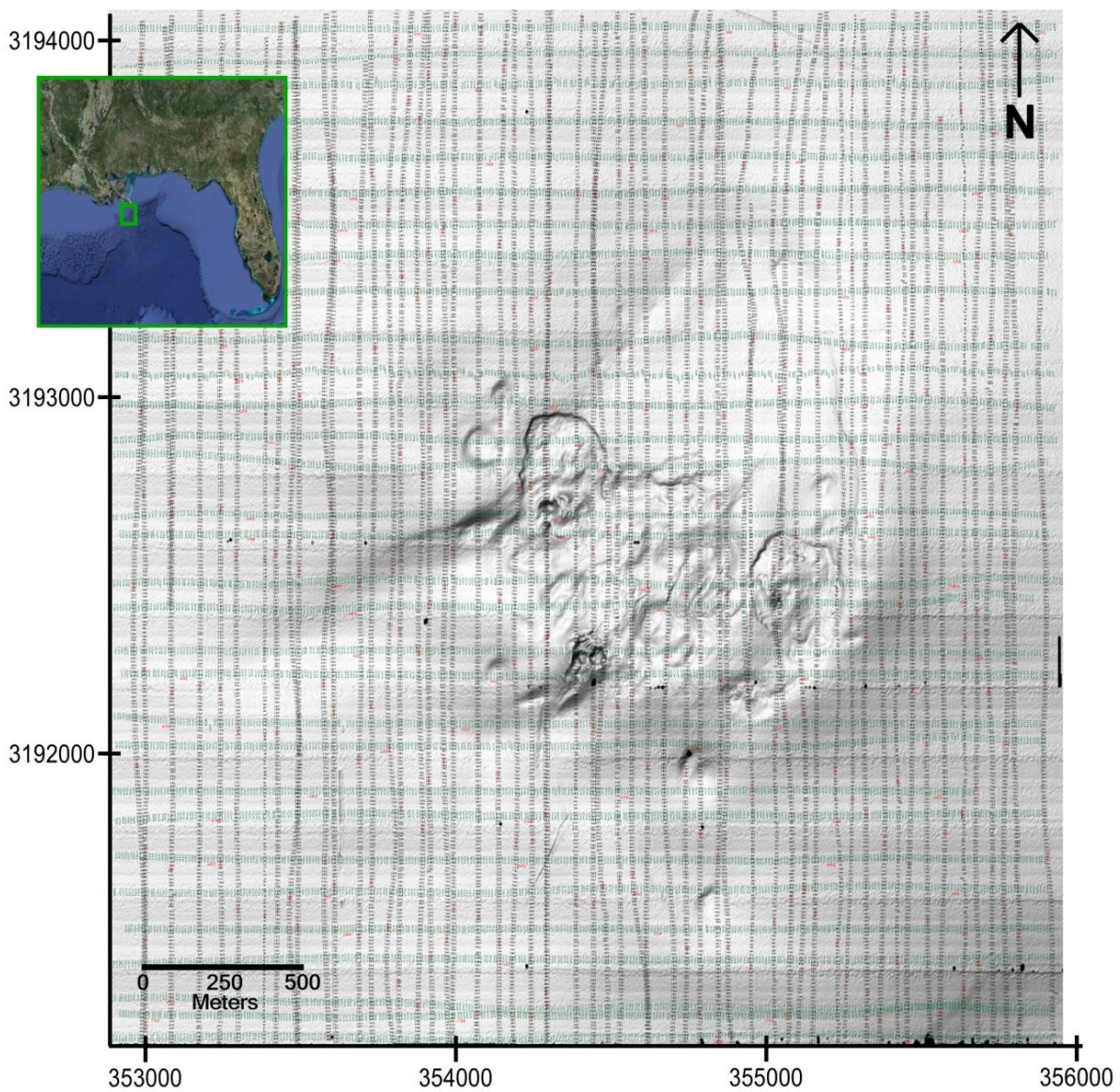


Figure 11: AUV-borne multibeam bathymetry map collected by Sleeper et al., 2006 overlain by the SSDR 3D grid.

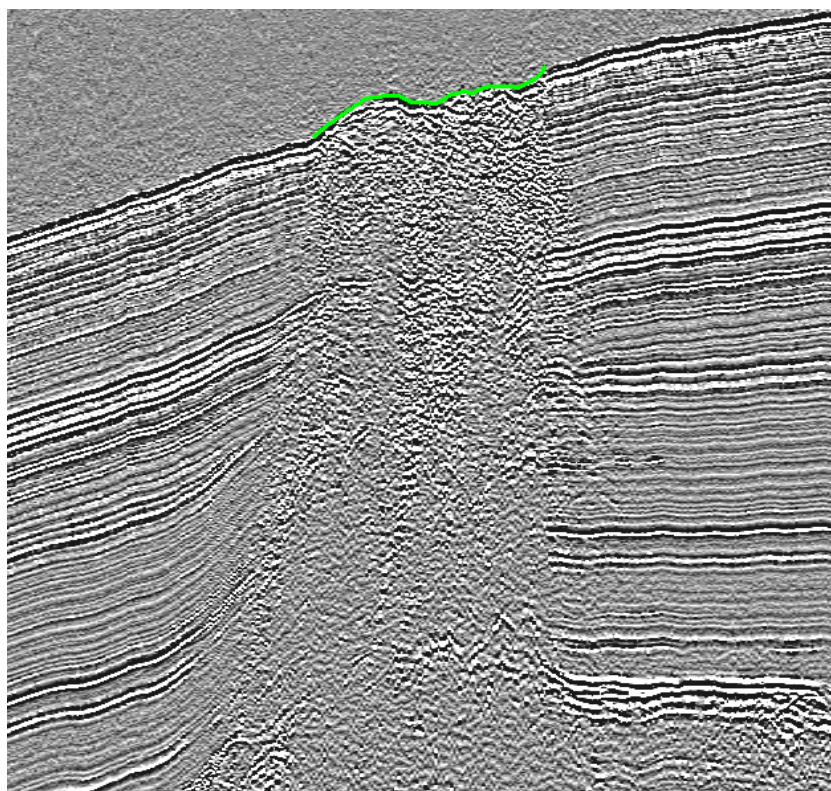


Figure 12: The high-scatter zone beneath Woolsey Mound. This is a representative inline from the SSDR survey completed by McGee et al. 2008 and Woolsey Mound is highlighted in green. Strong reflectors can be seen across the figure except for directly beneath the mound, which is a high-scatter zone.

High-Resolution Seismic and Core data

Simonetti et al. (2013) investigates the subsurface of Woolsey Mound using, primarily, the SSDR data. Jumbo piston cores were also collected to provide ground-truth for the seismic interpretation, by comparing the core data extracted in areas identified in the SSDR data as having high frequency scatter. The goal of coring at the sites was to substantiate the hypothesis that where there is an absence of coarse-grained sediments in the shallow subsurface, gas hydrates will only form and accumulate along fault segments that intersect in-transit thermogenic gas, which is mature gas of higher density, which, because of high diffusability, migrates upward (Max et al., 1997). They

found that gas hydrates occurred in massive fracture lenses and vein-filled fractures within fine-grained sediments. Simonetti et al. (2013) postulate that high frequency scattering anomalies present on the SDDR data may be a seismic signature of heterogeneous hydrate accumulations in fracture porosity. They also concede that hydrates appear to be preferentially distributed along segments of faults. These faults are both reservoirs and migration pathways for gas and gas hydrates.

Resistivity Data

Direct Current Resistivity Method

The Direct Current Resistivity (DCR) method is based on measuring electrical potential (voltage) between one or more electrode pairs while measuring the direct current between another electrode pair (Roy, 1971). Ground resistivity is related to various geological parameters such as mineral and pore fluid type, porosity, and the degree of water saturation in the rock (Loke, M.H., 2010). The fundamental physical law used in resistivity surveys is Ohm's Law in continuum form (Loke, 2010) because it has the form of Poisson's equation,

$$\frac{1}{\rho} \nabla^2 V = I \delta(x_0, y_0, z_0), \quad (3)$$

where V is voltage, I is current, and ρ is resistivity. The Dirac delta function on the right side has a volume of one at the point (x_0, y_0, z_0) and is zero elsewhere. It is used here to indicate that all the current (I) flows through the point (x_0, y_0, z_0) . In this way we are able to represent electrodes as points.

Once the resistivity data are collected, an inversion method is used to determine the solution for the measured resistivities. The goal of all inversion methods is to

determine a model of the subsurface whose response matches the measured response (Loke, 2010). Resistivity inversion is based on Poisson's equation. The subsurface is subdivided into discrete cells, and then an iterative process is used to find the cell resistivities for which Poisson's equation best predicts the observed resistivity measurement between successive electrode pairs. Given the fundamental ambiguity of hydrate saturation estimates based on resistivity alone, efforts have been made to incorporate additional parameters.

In this study a modified gradient electrode array configuration was used. The Gradient Array consists of positive and negative source electrodes at either end of a linear array, with multiple (9) receiver electrodes evenly spaced between (Loke, 2010) (Figure 13).

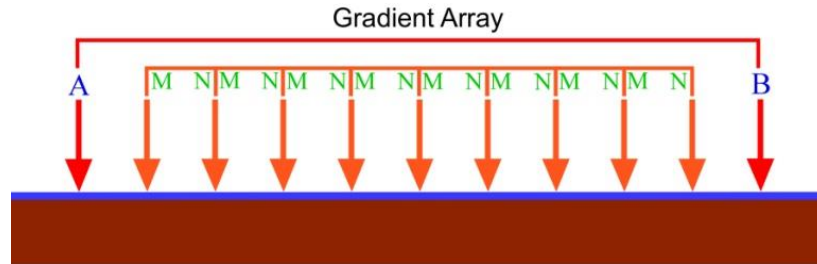


Figure 13: Gradient array schematic. 'A' is the positive current electrode position. 'B' is the negative current electrode. 'N' and 'M' are the pairs of recording electrodes.

For each channel, the basic measurement consists of the electrical potential difference (volts) between adjacent receiver electrodes divided by the current injected between the two source electrodes (amperes). For given current level, the voltage measured between potential electrodes is proportional to the average resistivity in the region surrounding the electrodes. The size of the region that influences the potential resistivity increases with increasing electrode separation. Seawater has a resistivity of

approximately 0.3 ohm-m and seafloor sediment average from 1 to 10 Ohm-m, which is 10 to 100 times smaller than typical resistivities measured on land or in freshwater. This means that the voltages measured between potential electrodes will be one to two orders of magnitude smaller than those that would be recorded on land, with the same level of injected current and the same offsets. Another difficulty for the acquisition of resistivity measurements on the deep seafloor is that the instrument and array must be built to function at water depths of a kilometer or more and to withstand the tension of a cable being dragged along the bottom. The gradient array was selected for use in this study because it provides the deepest penetration and highest voltage levels for multi-receiver pair arrays of a given length.

In Riedel et al. (2006), the authors monitored changes in sediment electrical resistivity at the southern Hydrate Ridge off Oregon. They performed controlled disassociation experiments on two cores filled with gas hydrate bearing sediments. They found that when gas hydrate is present in the sediments, electrical resistivity is significantly increased (Figure 12). While others report the same conclusion (Pearson et al., 1983; Hyndman et al., 1999; Collett and Ladd, 1999; Collett, 2001), Riedel et al. (2006) determined the sediment resistivities for different percentages of dissociated gas hydrate of these two cores (Figure 14).

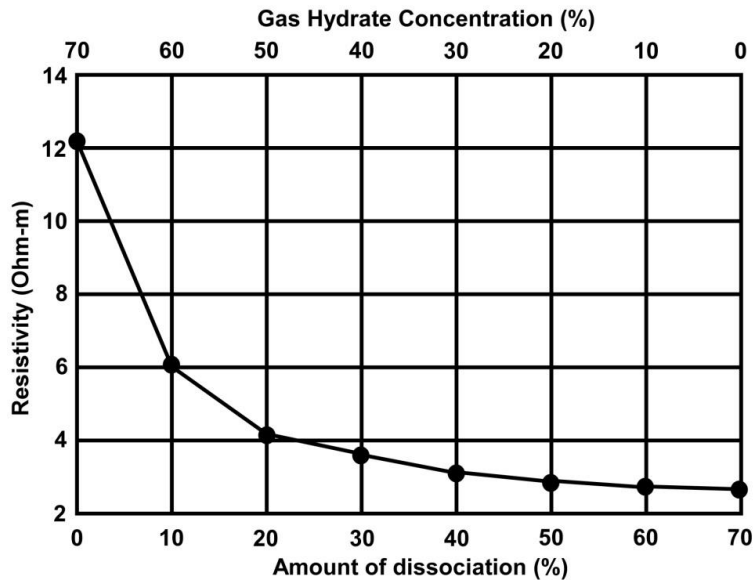


Figure 14: In situ hydrate concentration modified from M. Riedel et al. (2006). This figure shows in situ hydrate concentration at southern Hydrate Ridge off Oregon reported by Riedel et al. (2006). They identified changes in sediments electrical resistivity during three controlled gas hydrate dissociation experiments. They took cores from three locations and depths ranging from 3 meters below seafloor (mbsf) to 42.1 mbsf.

System Configuration and Acquisition

A study conducted by Dunbar et al. (2010) introduced a resistivity technique that involved towing an electrode array along the seafloor behind an underwater remotely operated vehicle (ROV). This resistivity system is based on an existing engineering-scale land system. The resistivity instrument is attached to the cage of an ROV and power is supplied by the large ROV battery (Figure 15).

During resistivity data acquisition, the ROV is towed 5-20 m above the seafloor through the water (Figure 16). A 1.1 km long, 56-electrode array is attached to the frame of the ROV and trails behind as the ROV is towed through the water. Because the array has slightly negative buoyancy, the active portion of the array drags along the seafloor. In the seawater environment, physical contact with the seafloor is not necessary, but

having the array on the seafloor rather than floating in the water column constrains its vertical location and minimizes its distance from the hydrate objective.

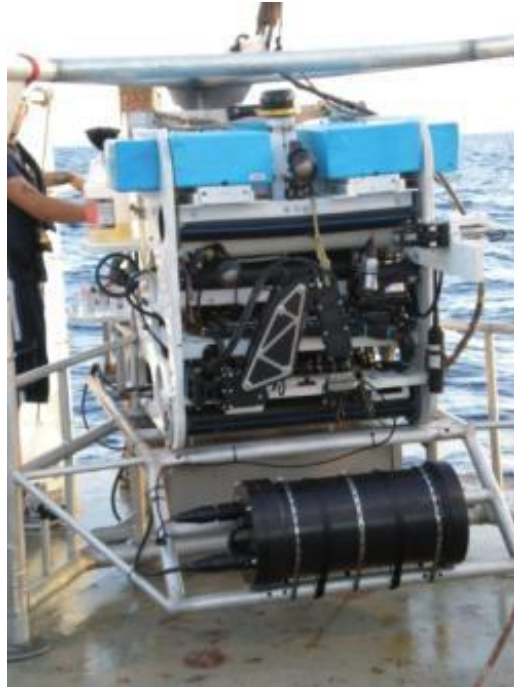


Figure 15: ROV and Converted SuperSting™ DCR system (Dunbar et al., 2010). This figure is two-fold. First the ROV is used for support of and as the power source for the DCR system, which sits within a frame. The DCR instrument is the black cylinder located on the front of the frame. On the back side of the frame the cable was attached and was allowed to drag along the seafloor. The instrument was towed between 5 and 20 meters above the seafloor and pulled through the water column at a speed of approximately 1 knot. This depth was intended to provide ideal coupling between the seafloor and the electrodes. The slow tow speed allowed high spatial sampling along the resistivity profile. With this setup the instrument and the 1.1 km long array were pulled along the bottom for a total 26.4 km.

The system has eight channels, which allows voltage to be measured between up to eight pairs of electrodes at one time and a pair of injector electrodes. The instrument is a converted Advanced Geosciences, Inc. (AGI) land instrument, model SuperSting R8/IP+56 adapted for use on the deep seafloor. This adaptation allows for continuous resistivity profiling (CRP) as well as stationary profiling at water depths of approximately 1000 meters. Graphite electrodes are spaced every 20 meters along the 1.1 km length of the array.

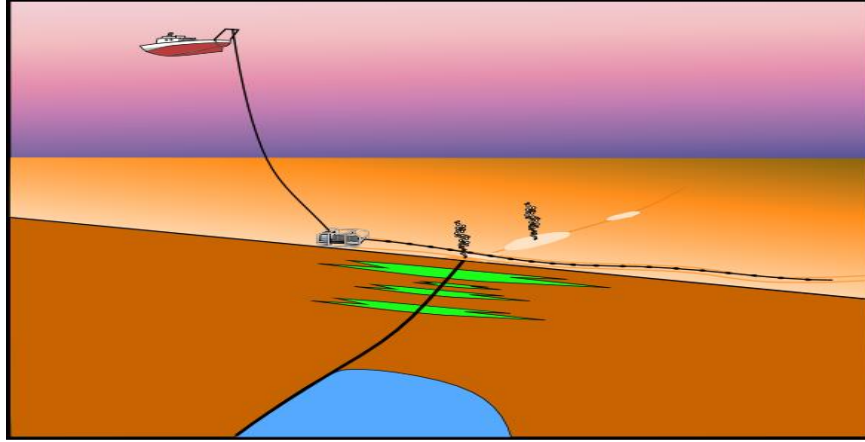


Figure 16: A cartoon of the DCR array (Dunbar et al., 2010). The array is pulled along the seafloor, while the resistivity instrument is pulled along just above the seafloor in the water column. The cartoon also shows a conceptual distribution of methane hydrate.

This electrode spacing provides resolution and depth of penetration of approximately 20 percent of the total offset. The acquisition time for each measurement is approximately 2.4 s, during which a 2 amp current is injected into the seawater between the A and B electrodes at either end of the array (Figure 13). The polarity of the A and B electrodes is then reversed, and the injection is repeated. These measurements are subtracted and the result recorded, so that any DC bias due to low frequency electrical noise is removed. The CRP data collected on June 5-6, 2009 represent more than thirty hours of continuous acquisition, totaling 26.4 km of profile data. Seven gradient arrays were collected in a repeating sequence of 200, 400, 600, 800, and 1000 m (Figure 17). The location of each measurement was extrapolated from an ultra-short baseline acoustic tracking system mounted to the ship identifying the location of the ROV on the seafloor. The array was assumed to follow the course of the ROV, as it trailed along behind.

A deep seafloor DCR survey of this scale, using this type of equipment, had not been attempted previously. The first objective, therefore, was to determine the extent to which valid resistivity data could be collected on the seafloor. Seawater-saturated

sediment in this area is expected to have resistivity greater than 1 Ohm-m and the hydrate-bearing sediment saturation to be even higher. Apparent resistivities less than 0.36 Ohm-m (resistivity of seawater) are highly unlikely. Apparent resistivities are a measure of the average resistivity encountered by current flowing between the source and receiver electrodes. Negative resistivities are not physically realistic because apparent resistivities are field measurements geologic properties.

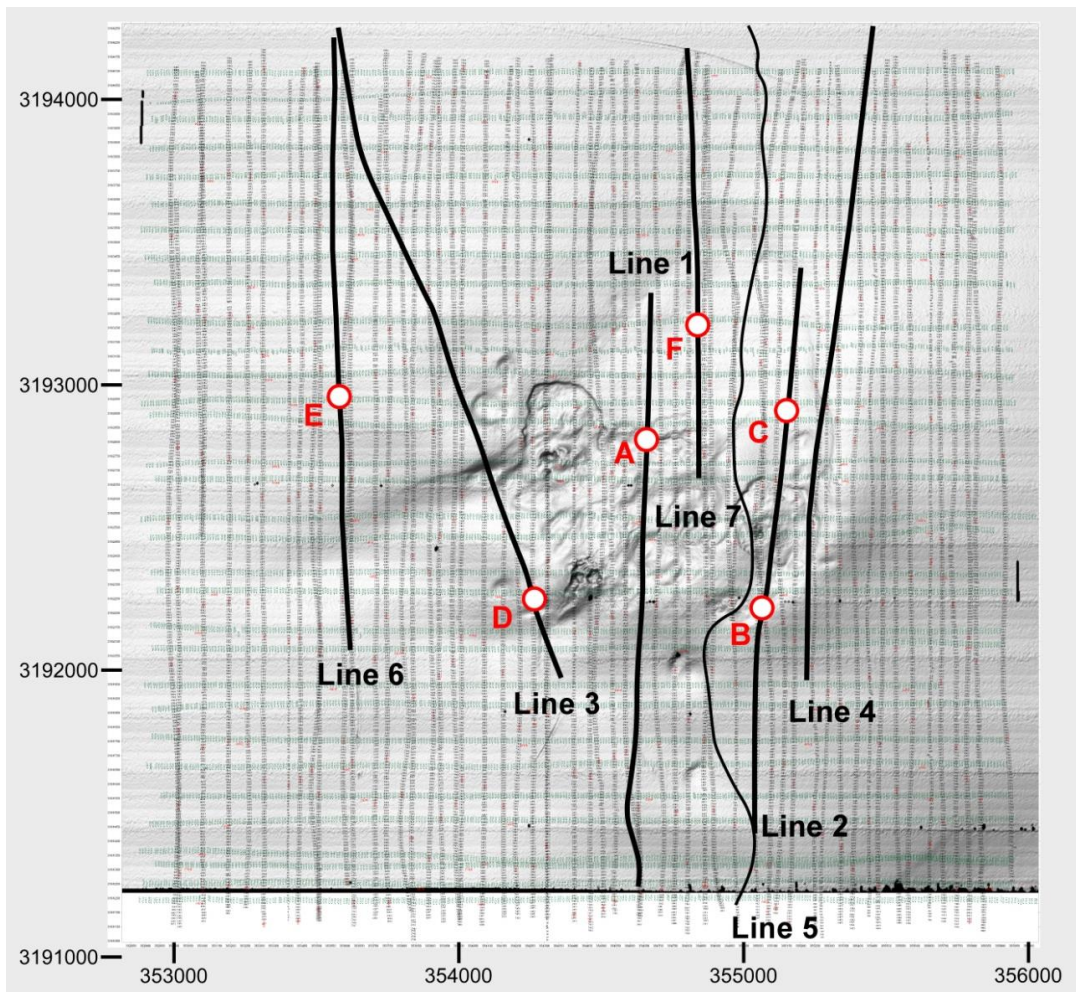


Figure 17: Overlay of the seismic inlines and crosslines along with the locations of the DCR profiles, modified from Dunbar et al. (2010). This diagram also highlights locations along DCR profiles of imaged high and intermediate resistivity values.

However, during the collection of resistivity data, some negative apparent resistivity measurements were recorded. Most of the negative resistivity measurements were recorded at large electrode offsets and likely correspond to electrical noise and current leakage in cable connectors. Negative apparent resistivities were removed from the data set prior to further processing. Statistics of the raw measurements over the entire survey by electrode offset versus channel number also showed issues with channels one and two and therefore all measurements taken on those channels were removed. Along with those faulty channels, offsets of greater than 600 m (including the 800 and 1100 m offsets) were not valid. Those far offset measurements were also removed from the data set. Despite those issues, a large data set was still available and the inverted cross sections of the mound at MC118 are likely representative of the sub-bottom resistivity distribution at the time of the survey.

For the majority of resistivity surveys, something is known about the geology of the subsurface *a priori* (Loke, 2010). In order to narrow the range of possibilities based on the known geology properties, other assumptions are made concerning the nature of the subsurface. The seafloor topography was constrained from an independent seafloor multi-beam survey acquired by another group (Figure 7). The resistivity of the seawater was constrained to an average value determined from a vertical conductivity profile through the water column collected on the same day as the DCR survey. The conductivity profile was acquired on the same day to ensure the most current value. The resistivity of the sub-bottom was constrained to be within 0.3 and 100 Ohm-m. These assumptions are incorporated into an inversion of the acquired resistivity measurements. A least squares inversion is performed using the combination of these assumptions and

the application of smoothing and damping parameters. For any measured data set, there are an infinite number of models that satisfy the apparent resistivity values. The inversion that produced the smoothest model that fits the measured apparent resistivity values acceptably was found. This model is used to identify likely zones of high hydrate saturation within the sediments beneath Woolsey Mound.

Results of the DCR Survey

Two DCR lines from Dunbar et al. (2010) were used in this study. The first of these two lines is located on, and extends over, the central flank of Woolsey Mound (Figure 18). This area is near the location where massive blocks of hydrate have been observed protruding from the seafloor. The largest anomaly (marked 'A') seen in this study occurs in a location along a known north-dipping normal fault. This anomaly is 100 Ohm-m and extends to about 50 meters below the seafloor.

The second line is to the east of the center of Woolsey Mound and extends across an old vent (Figure 19). Much of the southern portion of the line is underlain by irregularly shaped resistivity anomalies ranging from 1 to 3 Ohm-m. There are two exceptions marked 'B' and 'C' in figure 19. At anomaly 'B' there is another 100 Ohm-m region that extends to 30 meters below the seafloor. This coincides with the a second deep-seated north-dipping normal fault. Anomaly 'C' is a 3 Ohm-m section that extends from the seafloor to 100 meters depth. This anomaly is located along the same deep-seated fault seen along the first line where anomaly 'A' is seen.

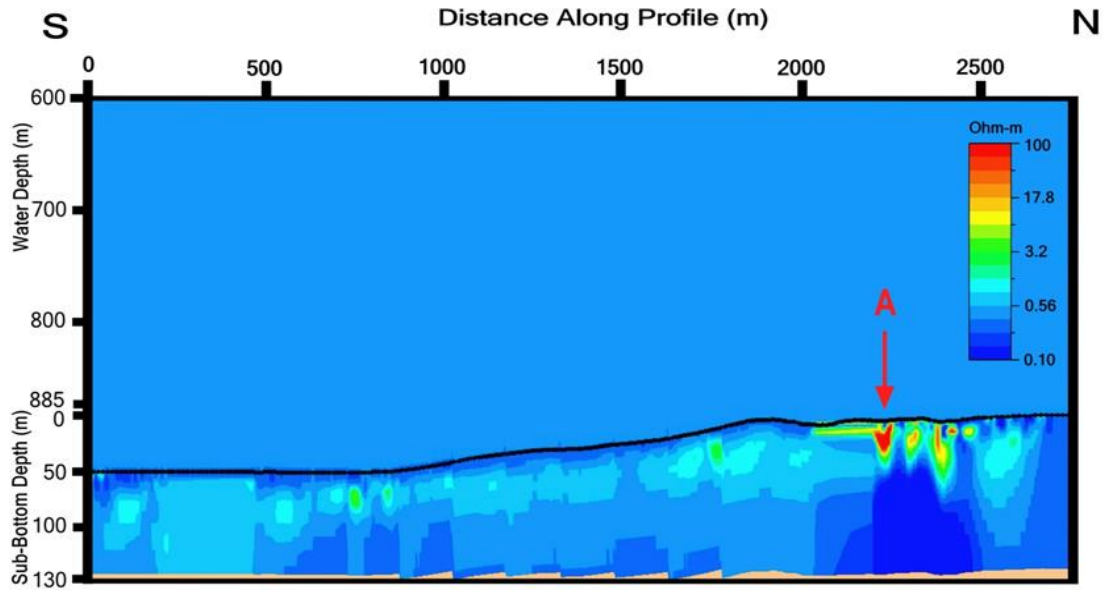


Figure 18: DCR Line 1 that is located on and extends over, the central flank of Woolsey Mound. The largest anomaly (Marked 'A') seen in this study occurs in a location along a known north-dipping normal fault. This anomaly is 100 Ohm-m and extends to about 50 m below the seafloor. Other high resistivity anomalies are also seen to the north.

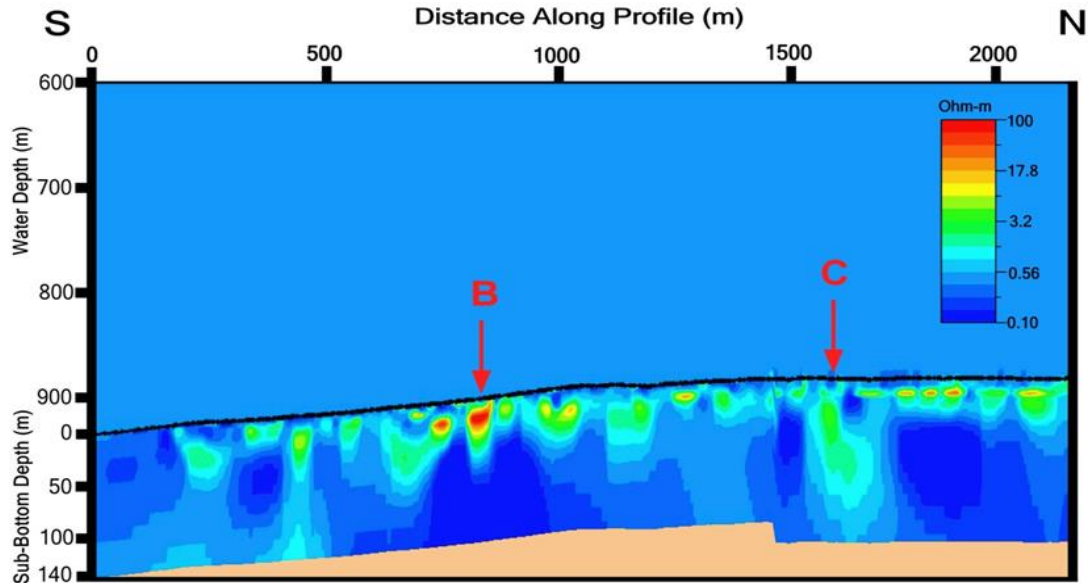


Figure 19: This line is to the east of Woolsey Mound and extends across what appears to be an old, inactive vent. There are two exceptions marked 'B' and 'C'. At anomaly 'B' there is another 100 Ohm-m region that extends to 30 meters below the seafloor. Anomaly 'C' is a 3 Ohm-m section that extends from the seafloor to 100 meters depth. This anomaly is located along the same deep-seated fault seen along the first line where anomaly 'A' is seen (Figure 18).

CHAPTER THREE

Methods

Seismic Attribute Analysis

A suite of seismic attribute analyses was computed across the SSDR seismic data using Kingdom Suite™ software, by Seismic Micro Technology, ASIA PTE, Ltd.

Seismic attributes are quantities computed from seismic amplitude traces that potentially provide different or additional information that is not apparent from the seismic amplitude traces alone (Taner et al., 1979). Seismic attribute analyses are generally used for lithological and petrophysical prediction of reservoirs and various methodologies have been developed for their application to hydrocarbon exploration and development (Chopra and Marfurt, 2006). In this study, seismic attribute tests were conducted to determine what additional information could be gleaned from the SSDR data about the hydrate distribution beneath Woolsey Mound. Several attributes were tested (average energy, instantaneous phase, amplitude envelope, instantaneous frequency, Hilbert transform, and one-dimension seismic inversion) to determine if any of these could be used to identify the hydrate deposits (Figure 20).

Average Energy is defined by Barnes (2007) to be the total energy of the trace divided by the number of samples, or the square of the rms amplitude

$$E = \frac{1}{N} \sum_{n=1}^N x_n^2, \quad (4)$$

where E is the total energy, N is the number of samples, and x is the rms amplitude.

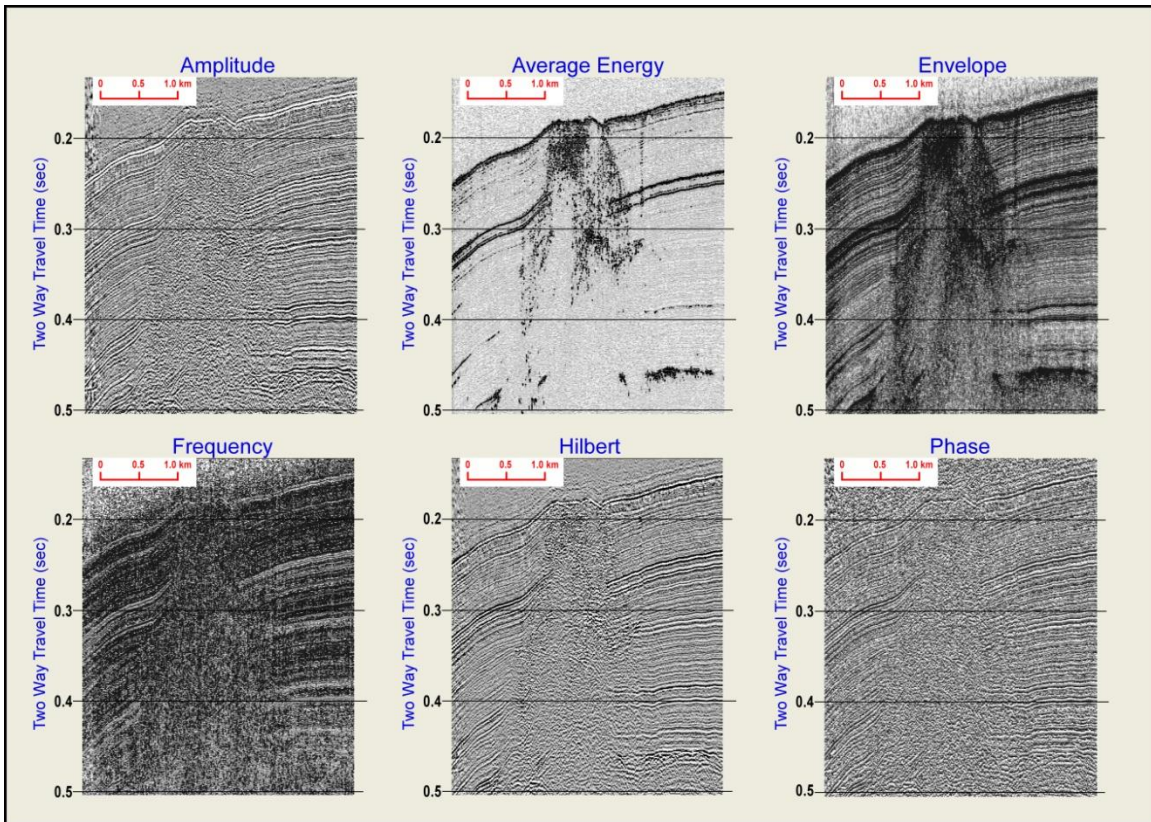


Figure 20: Different seismic attribute profiles of a representative inline. Five of these analyses were performed for the two intersecting SSSR inlines.

The Hilbert transform is a process that creates a new quadrature or imaginary trace by rotating the phase of each frequency component of the input (real) seismic trace by 90 degrees (Luo et al., 2003). Instantaneous frequency is the first derivative of the phase; it is often used to detect gas but is less reliable than other approaches (Brown, 1994). The amplitude envelope attribute (also called reflection strength) is a measure of reflection amplitude that is insensitive to phase (Chopra and Marfurt, 2008). Instantaneous phase enhances the continuity of events by ignoring the amplitude information in time samples (Chopra and Marfurt, 2005).

Once these seismic attributes were computed, the best attribute for identifying areas of high hydrate saturation was identified by visually comparing the attribute sections with near-coincident resistivity profiles. The goal was to find the attribute that best correlated, either positively or negatively, with the high resistivity anomalies. In this sense, the resistivity data were used to calibrate the seismic attribute data for hydrate occurrence. Once a visual correlation was found, the difference between the mean values of the candidate attribute within and outside the region of high resistivity was computed to check for statistical validity. The values for this computation were gathered by choosing random locations along the two seismic profiles, both inside and outside the anomalous regions. The 95% confidence interval for the difference of the means of these sample sets is

$$(\bar{x}_1 - \bar{x}_2) - z_{\frac{\alpha}{2}} \sqrt{\frac{\sigma_1^2}{n_1} + \frac{\sigma_2^2}{n_2}} < \mu_1 - \mu_2 < (\bar{x}_1 - \bar{x}_2) + z_{\frac{\alpha}{2}} \sqrt{\frac{\sigma_1^2}{n_1} + \frac{\sigma_2^2}{n_2}}; \quad (5)$$

where \bar{x}_1 and \bar{x}_2 are means of independent random samples of size n_1 and n_2 from populations with known variances σ_1^2 and σ_2^2 respectively. $z_{\frac{\alpha}{2}}$ is the value of the standard normal curve leaving an area of $\frac{\alpha}{2}$ to the right (DeVore, and Farnum, 2005). By making comparisons, both quantitative and qualitative, the seismic attribute that was the best at isolating the anomalous regions observed in the seismic data was selected.

Combination of DCR with SSSR Data

The resistivity and seismic profiles are not perfectly parallel, so they are projected onto a common line. Perpendicular projection is used to superimpose the resistivity onto the seismic data. The perpendicular projection is applied to distances along the profiles that do not exceed 25 m. This is reasonable because the DCR data are influenced by resistivity variations within a cylinder around the electrode array with a radius approximately equal to 20% of the maximum electrode offset (in this case 20% of the total offset is 220 meters). Each seismic attribute inline section was overlain by the nearest DCR line to determine which attribute best correlated with the resistivity anomalies. An inline section is the north-south seismic line of the seismic grid (Figure 11). Using this approach, DCR line 1 was compared to seismic inline section number 27 and DCR line 2 is compared to seismic inline section number 18 (Figure 21). Two additional DCR lines were available for evaluation, but these lack significant resistivity anomalies and no further comparisons were made.

The distribution of hydrate beneath the Woolsey Mound was interpreted by identifying seismic attribute patterns that correlate with resistivity anomalies. There are two correlative zones where the seismic attributes and resistivity anomalies could be mapped. In response to the limited number of DCR profiles available to match with the SSSR data, the extent of seismic attributes values that correlate with high resistivity anomalies was mapped over the remaining seismic inline and crossline sections. Once the anomalous zones were traced across each applicable inline and crossline section, all the mapped zones of anomalous scatter were overlain. The areas of dense overlap for

each correlative feature were then used to make inferences of the methane hydrate distributions beneath Woolsey Mound.

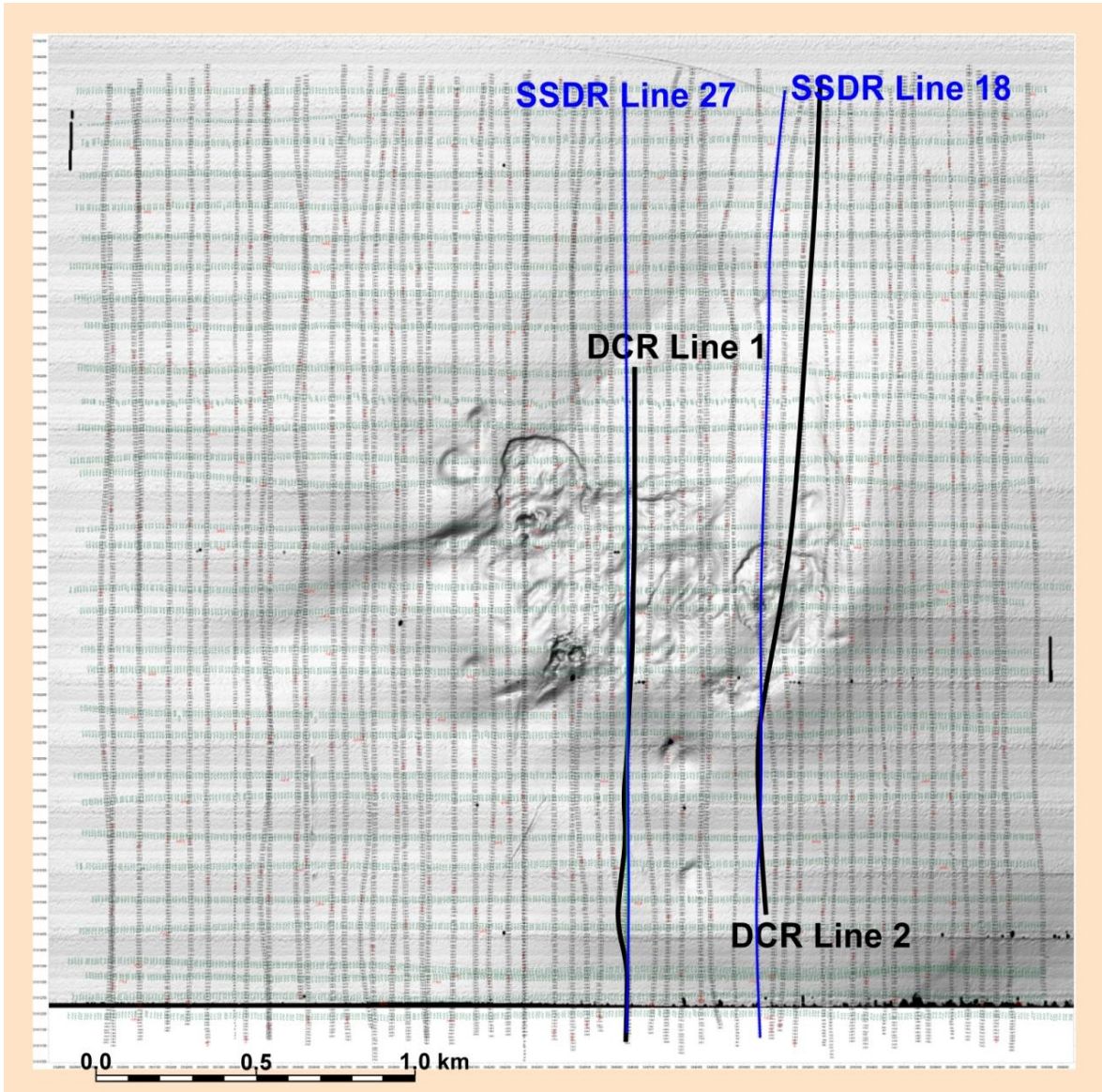


Figure 21: SSDR survey lines overlain by DCR Lines 1 and 2.

CHAPTER FOUR

Results

Seismic Results

SSDR Lines 27 and 18 are highlighted in this study because of their proximity to DCR profile 1 and 2. The amplitude attribute profiles of these lines show a zone of scatter directly beneath Woolsey Mound, which masks any coherent reflections. In light of this scatter zone, it was apparent that additional analyses were needed to glean additional information from these seismic data.

The additional seismic attribute analysis produced mixed results. In general, all but two of the seismic attributes identified additional information for the scatter zone beneath Woolsey Mound. These two seismic attributes are the average energy and amplitude envelope attributes. Upon the completion of the different attribute analyses, the average energy attribute offered the most identifiable characteristics that could be used for comparison to the DCR data. The envelope attribute did enhance the seismic reflectors within the scatter zone, but did not add any additional clarity above what was shown with the average energy attribute. The average energy attribute is able to resolve two zones beneath Woolsey mound. These zones are a high average energy zone (outlined in blue) and a low average energy zone (outlined in yellow) (Figure 22).

The difference between high and low average energy zones are identifiable visually by the high scatter content in the high average energy zones and the absence of scatter in the low average energy zones. The difference between high and low average

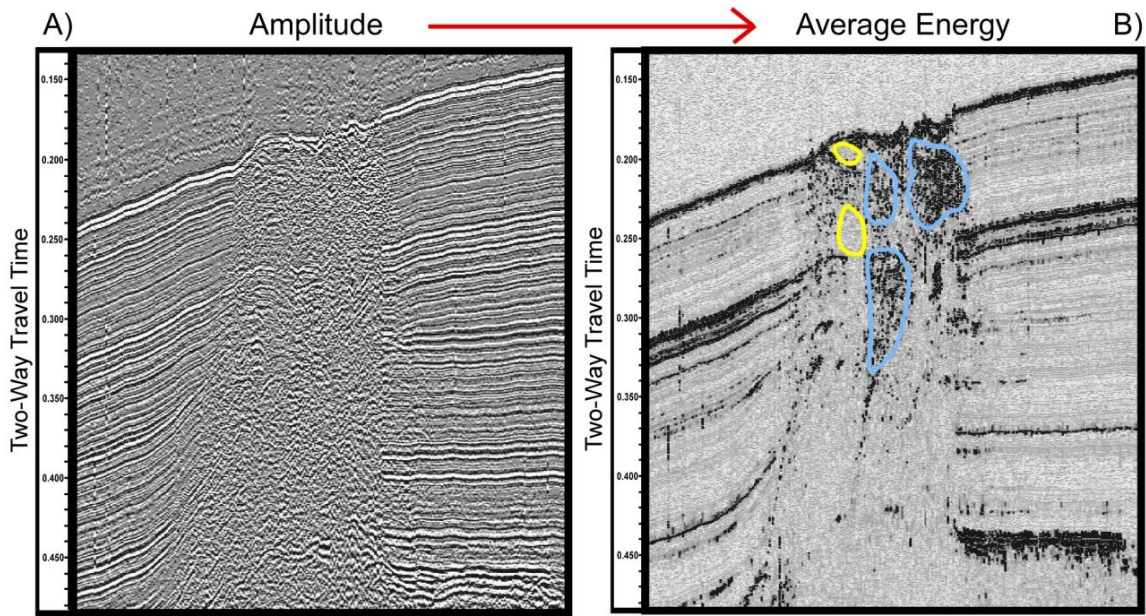


Figure 22: A SSDR inline across the active vent on Woolsey Mound. A) The amplitude profile of that line and B) the average amplitude attribute for the same line. The seismic profiles are displayed in two-way-travel time (TWT) and depth using an assumed velocity of 1500 m/s. The yellow circles are highlighting those areas of low average energy. The blue circles highlight the high average energy scatter.

energy attribute values on the two lines is 4.9 ± 0.46 . 4.9 at 95% confidence, for both SSDR Line 27 and 18 and is therefore statistically significant. The high average energy for both SSDR Lines 27 and 18 is almost exclusively limited to the zone beneath Woolsey Mound extending to depths greater than 50 meters in some locations. The zone of low average energy can be seen across the entire seismic profile extending to depths less than 50 meters below the water bottom. Scattered energy levels are expected to decrease with depth by the normal processes of spherical spreading and intrinsic attenuation. Hence, only those anomalous low average energy zones beneath the mound and surrounded by high average energy zones are mapped.

A series of conclusions can be drawn from the graphic overlay of the SSDR Lines and the DCR profiles. First, when DCR profiles are overlain onto adjacent SSDR Lines,

zones of low average energy correspond to high resistivity zones, surrounded by zones of high average energy beneath Woolsey mound. Second, in the same manner as above, zones of intermediate resistivity correspond to the zones of high average energy beneath Woolsey mound.

SSDR Line 27

The amplitude attribute profile for SSDR Line 27 shows coherent reflections adjacent to Woolsey Mound, but clear definition of the reflections beneath are masked by a scatter zone that extends from the seafloor to the base of the seismic record (Figure 23).

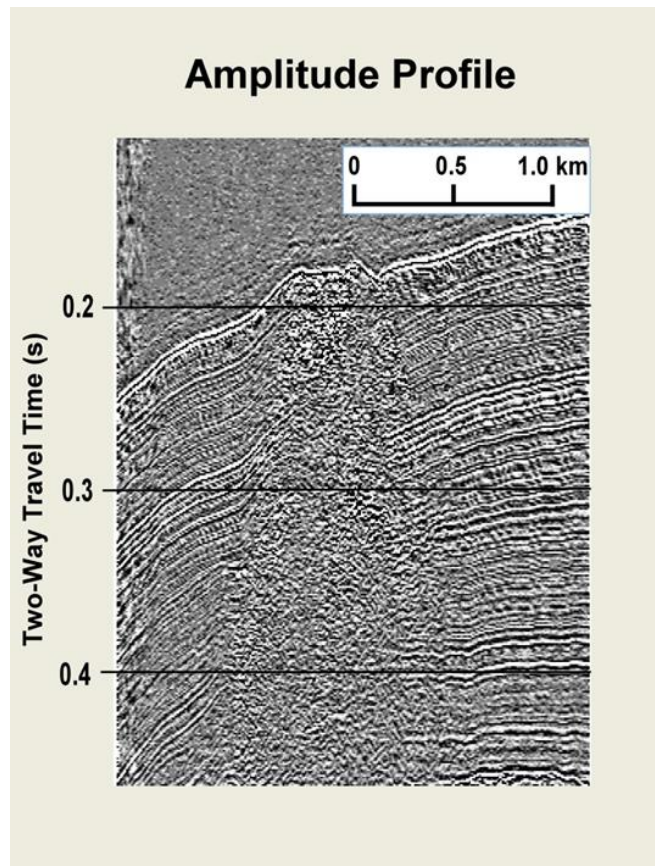


Figure 23: SSDR Line 27 amplitude seismic attribute profile. The seismic profiles are displayed in two-way-travel time (TWT) and depth using an assumed velocity of 1500 m/s.

The instantaneous phase attribute profile is a rotation of the phase spectrum by 90°. This phase rotation diminishes the continuity of the reflections, where they are visible adjacent to the mound, and has little effect on the data beneath the mound (Figure 24).

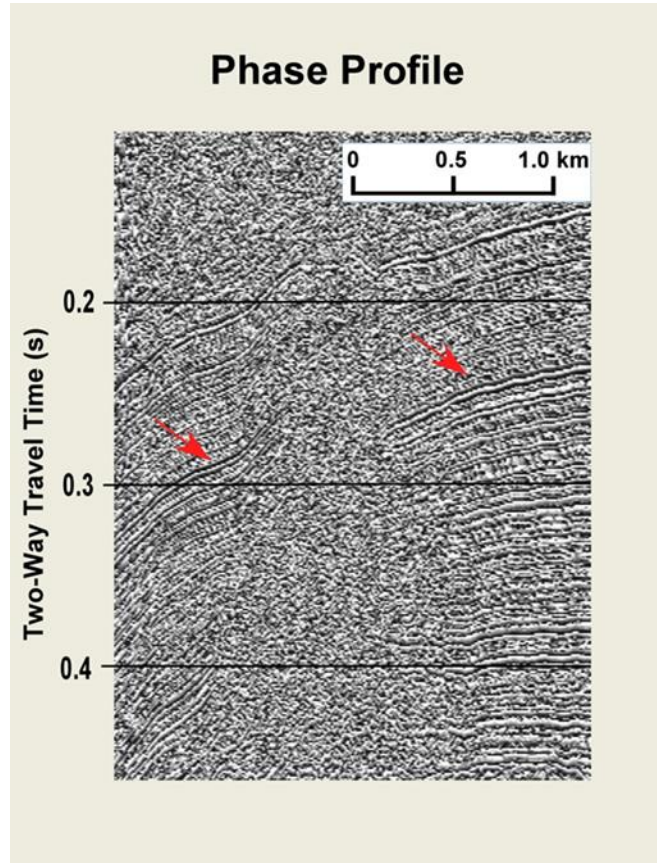


Figure 24: SSDR Line 27 instantaneous phase seismic attribute profile. The seismic profiles are displayed in two-way-travel time (TWT) and depth using an assumed velocity of 1500 m/s. The red arrows are pointing to location of strong reflectors within the sediment column.

It is possible to identify many bedding plane reflections, up-dip and down-dip of the mound, but the only strong reflector that can be seen along the entire length of the line is the seafloor reflection.

The amplitude envelope attribute accentuates deeper bedding plane reflections, in particular the strong reflection imaged in the middle of the profile (Figure 25).

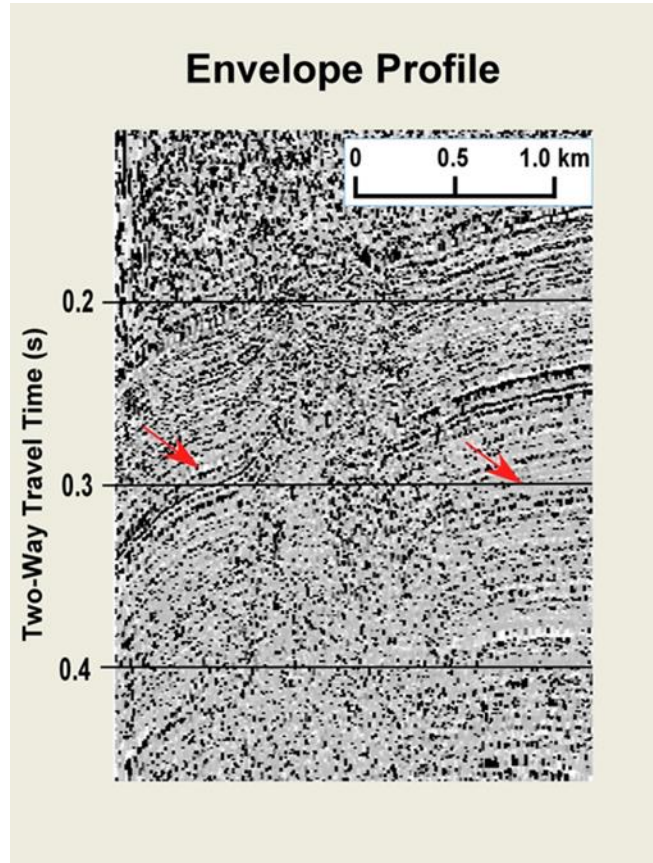


Figure 25: SSDR Line 27 amplitude envelope seismic attribute profile. The seismic profiles are displayed in two-way-travel time (TWT) and depth using an assumed velocity of 1500 m/s. The red arrows are pointing to location of strong reflectors within the sediment column.

The Hilbert transform attribute profile accentuates both shallow and deep bedding plane reflections and shows the extent of the scatter zone (Figure 26). The intensity of scatter beneath Woolsey Mound is shown to be highest in the first 0.1 s two-way travel time below the bottom and to diminishes with depth. It is also possible to make out locations that might be faults along the edges of the high-scatter zone on the Hilbert transform section.

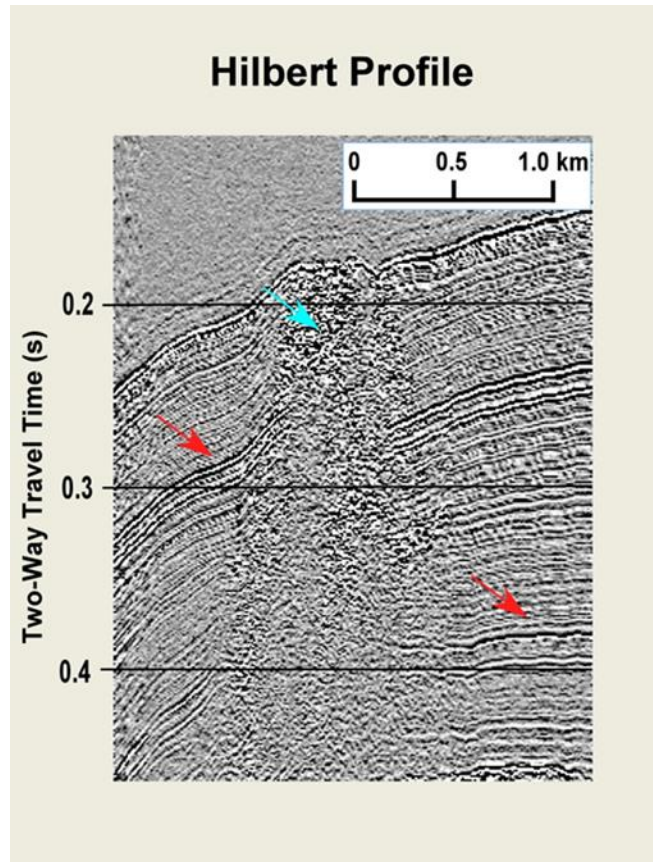


Figure 26: SSSR Line 27 Hilbert transform seismic attribute profile. The seismic profiles are displayed in two-way-travel time (TWT) and depth using an assumed velocity of 1500 m/s. Possible faults are highlighted in yellow. Strong reflectors are shown with red arrows. High scatter zones are indicated with a blue arrow.

The seismic inversion attribute profile intensifies the seafloor reflection, the scatter zone beneath Woolsey Mound, and the bedding plane reflections adjacent to the mound (Figure 27).

The average energy attribute diminishes the smaller bedding-plane reflections on SSSR Line 27 (Figures 28). It enhances two strong reflections in the middle of the seismic profile. The average energy attribute is also the best attribute for distinguishing variations in intensity of scattered energy beneath the mound. Zones of scattered energy are identified, with high and low intensity. The zone of low average energy is surrounded by high average energy particularly beneath Woolsey Mound.

Two faults are likely bracketing these zones, but their extent and true nature are difficult to discern from these data alone.

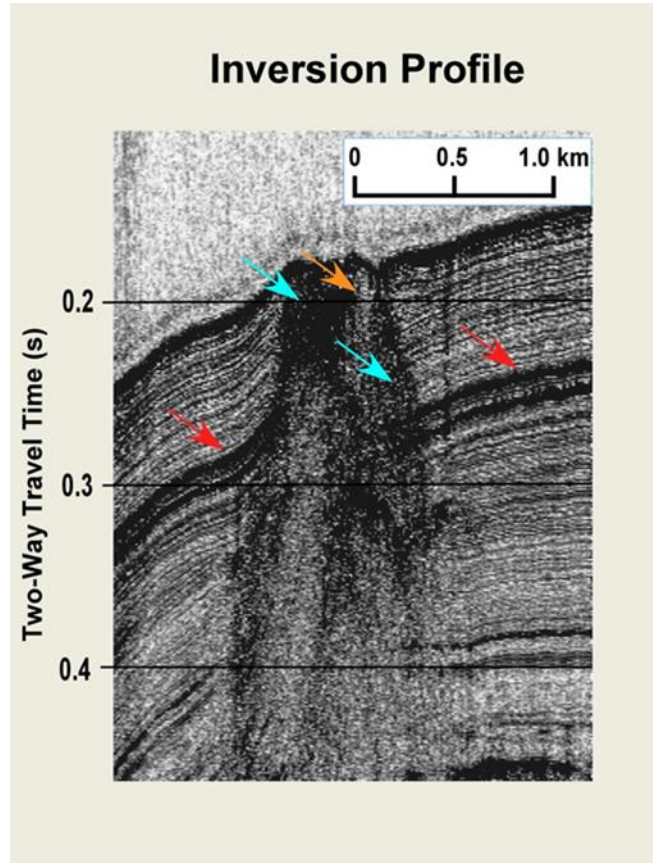


Figure 27: SSSR Line amplitude inversion seismic attribute profile. The seismic profiles are displayed in two-way-travel time (TWT) and depth using an assumed velocity of 1500 m/s. Scattered energy occurs all the way to the base of the seismic amplitude inversion attribute (blue arrow). However, this is not true for the entire zone beneath Woolsey Mound. There seem to be areas of scatter (blue arrows) that surround areas of little to no scatter (orange arrow). This distinction is not discernible on the other attribute sections. The locations of bounding faults (yellow lines) surrounding the scatter of energy can also be identified in the inversion profile.

SSDR Line 18

SSDR Line 18 crosses the eastern flank of Woolsey Mound, over inactive vents. Unlike SSSR 27, the seismic amplitude display shows bedding plane reflections both, adjacent to and beneath the flank of the mound (Figure 28). There is also a zone that has

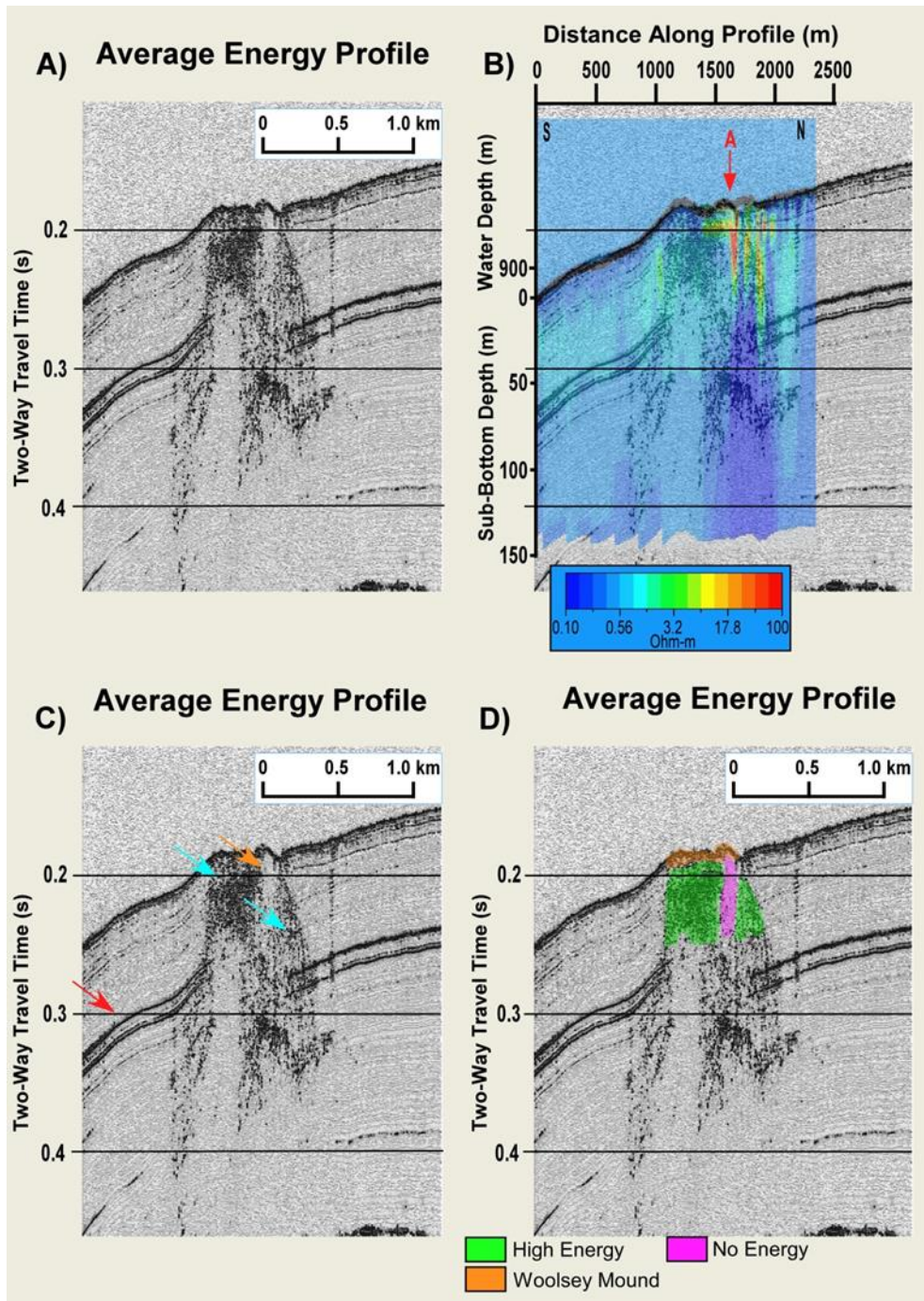


Figure 28: Interpretation of SSSR Line 27. The seismic profiles are displayed in two-way-travel time (TWT) and depth using an assumed velocity of 1500 m/s. A) Average energy seismic attribute inline view of SSSR Line 27. B) SSSR Line 27 average energy seismic attribute inline overlain by the DCR profile with a red arrow indicating a location of interest seen in the DCR data. C) SSSR Line 27 highlighting those locations of interest. The red line is pointing to a series of strong reflectors nearly continuous across the profile. The blue arrows are pointing to the high energy scatter beneath Woolsey Mound. The orange arrow is pointing to an area of little or no scattered energy. D) Interpretation SSSR Line 27.

subsidied and subsequently filled with younger sediments, indicating ongoing tectonic motion on the flanks of Woolsey Mound. The same analyses performed on SSSR Line 18 were applied here and the results were similar to those seen for SSSR Line 27.

The phase attribute profile does not clarify the structure any better than the amplitude profile. The envelope attribute profile accentuates deeper bedding plane reflections and the strongest reflection at about the middle of the profile. This attribute does little to clarify any other reflections in the profile. The Hilbert attribute profile makes it difficult to identify the strongest bedding plane reflectors and areas where deposition has occurred in an accommodation zone. It is difficult to identify the location of any scatter or shape of the high scatter zone. The inversion attribute profile accentuates the variation of the scattered energy within the high-scatter zone and bedding plane reflections. An accommodation zone and the faults that bracket the accommodation zone can be clearly identified. There are also other faults that can be seen on the southern (downslope) part of the section.

The average energy attribute profile accentuates patches of high-energy scatter directly beneath Woolsey Mound (Figure 29). There is also a linear zone of intermediate energy that extends along a fault south of Woolsey Mound. The extent and internal bedding within the accommodation zone, and the extent of the subsidence along the bound faults, can be seen. The seafloor bathymetric expression of Woolsey Mound is clearly seen and is bracketed by faults that extend to the base of this profile.

The average energy attribute matched best with the highly resistive zones beneath Woolsey Mound. The comparisons of the other seismic attributes do not increase the ability to glean additional information from these SSSR Lines, and alone, none of the

SSDR attribute analysis provides enough concrete information about sediment properties. Also based on the SSDR data alone, it is not possible to interpret the significance of the zones of low-scatter intensity, surrounded by high scatter. Coring beneath Woolsey Mound has produced sediment samples containing free gas from areas of high scatter (Simonetti et al., 2013). The areas of low-scatter intensity surrounded by areas of high scatter have not been cored, because they occur beneath areas where the bottom is covered by consolidated carbonate that cannot be penetrated by piston cores. Zones beneath Woolsey Mound that have high average energy in the SSDR data and have intermediate to lower resistivity values in the DCR data are highlighted in Figure 30.

Within these zones are the low average energy zones from the SSDR data and the high resistivity zones in the DCR data. These are also highlighted in Figure 30.

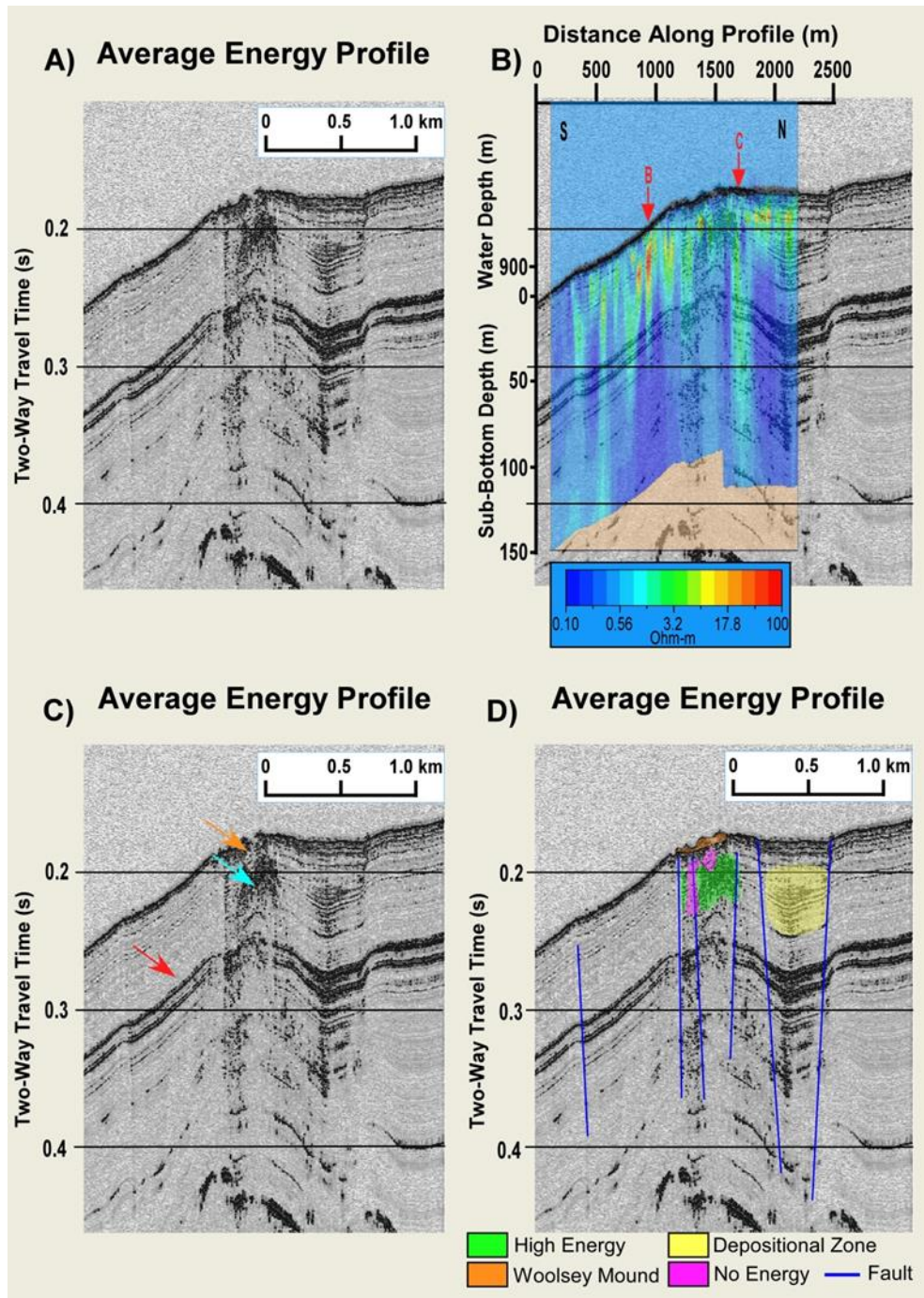


Figure 29: Interpretation of SSDR Line 18. A) Average energy seismic attribute inline view of SSDR Line 18. B) SSDR Line 18 average energy seismic attribute inline overlain by the DCR profile. C) SSDR Line 18 highlighting those locations of interest. The red line is pointing to a series of strong reflectors nearly continuous across the profile. The blue arrow is pointing to the high frequency scatter beneath Woolsey Mound. The orange arrow is pointing to an area of little or no scattered energy. D) This view is the interpreted SSDR Line 18.

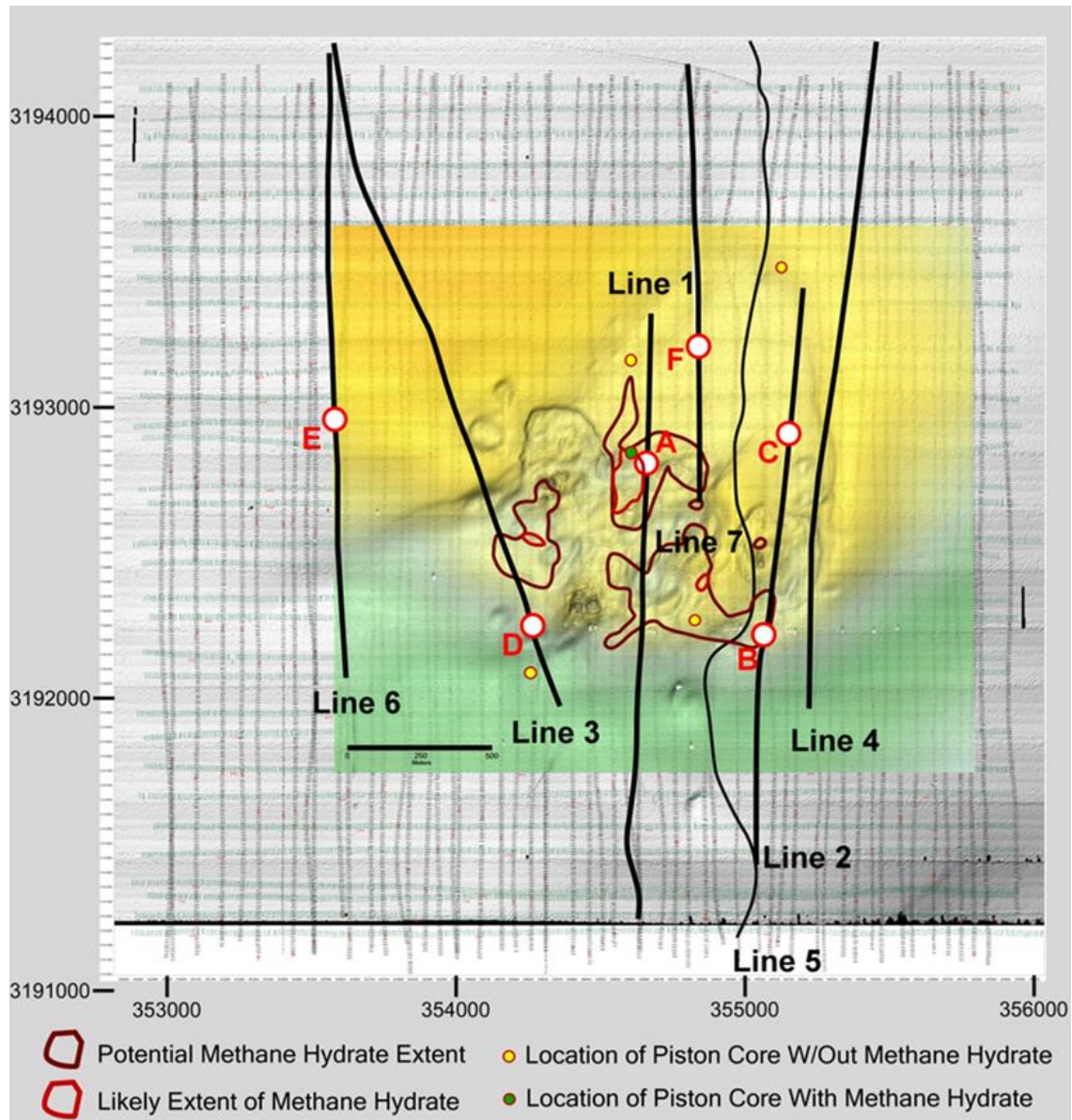


Figure 30: Proposed distribution of high saturation methane hydrate, Woolsey Mound, MC118, Gulf of Mexico. This figure includes the seismic inline and crossline locations covering Woolsey Mound. Those inlines and crosslines are overlain by a bathymetric profile of Woolsey Mound. The DCR survey lines are overlain in black. Areas from the DCR survey are also included in red and white circles. The extrapolated areas of high average energy and intermediate resistivity values are highlighted in brown (disseminated free gas). The extrapolated areas of no/low average energy and high resistivity values are highlighted in red (Methane hydrate). The circles mark the locations of piston core samples taken since this study was completed. These zones were chosen based on the DCR work along with other seismic interpretations and seafloor expression seen with underwater cameras. Those piston core locations with methane hydrate in the sample and those without any methane hydrate are identified by green fill.

CHAPTER FIVE

Discussion

Riedel et al. (2006) show that gas hydrate accumulation increases the resistivity values. They also indicate that approximately 55 % of dissociation produces a significantly large resistivity increase that can be identified. The intermediate resistivity values surrounding the areas of interest in the DCR data point to the likelihood of gas disassociation beneath Woolsey mound. These intermediate resistivity values are higher than the typical sediment resistivities adjacent to the mound and significantly lower than the isolated high resistivity anomalies. Riedel et al. (2006) did not identify resistivity zones greater than 12 Ohm-m (Figure 14), but in the survey conducted by Dunbar et al., 2010, zones of resistivity values reach 100 Ohm-m.

The graph of resistivity versus hydrate saturation by Riedel et al. (2006) indicates a resistivity of 12 Ohm-m for saturation of 70% (Figure 14). Hence, the 100 Ohm-m resistivities anomalies found by Dunbar et al. (2010) must correspond to gas hydrate at significantly high concentrations.

Exploration for hydrate with seismic data alone increases the difficulty of quantifying the amount of hydrate in a zone, especially with no well data (Edwards, 1997). Simonetti et al. (2013) showed that the inclusion of coring can add to the spacial distribution of methane hydrate beneath Woolsey Mound. They concluded that high frequency noise does occur along master faults associated with thermogenic gas conduits. Our study agrees with Simonetti et al. (2013). In our study the distribution of high

frequency scatter (high energy scatter) is seen to surround those thermogenic gas conduits. The inclusion of DCR data is also able to help refine the understanding of those high scatter areas acting as a proxy for well data.

In this study, we use resistivity data as a proxy for core samples from beneath carbonate rock to identify seismic scatter patterns associated with different concentration levels of hydrate and/or free gas. Not until the comparisons with the resistivity data are made can we start to identify properties related to the influence of methane hydrate and disseminated methane beneath Woolsey Mound and map those locations. There appear to be localized zones of high-saturation methane hydrate accumulation that has either been trapped beneath Woolsey Mound or is still ascending along faults or fractures. These localized zones may be surrounded by dissociation halos or zones of lower-saturation hydrate within the muddy sediments beneath Woolsey mound.

CHAPTER SIX

Conclusions

Active venting of free gas at a seafloor mound does not require solid methane hydrate blocks within shallow seafloor sediments. However, the presence of even small amounts of disseminated free gas and carbonate blocks on the seafloor and buried in the sediments absorbs and scatters seismic signal to the point that coherent reflections are not recorded beneath Woolsey Mound. The average energy seismic attribute of the SSSR data shows significant variation beneath the mound, but specifically what causes the variations cannot be understood without additional information. In this study the prior DCR survey provides that need additional information. The survey conducted by Dunbar et al., 2010 identified high (100 Ohm-m) and intermediate (10 to 70 Ohm-m) resistivity values that are consistent with previous methane hydrate work.

The extent of methane hydrate found beneath Woolsey Mound can be determined by combining seismic attribute analysis and DCR inversions of the near seafloor sediments beneath this active methane hydrate mound. The mapping done based of the combination of these geophysical techniques highlights the likely positions of methane hydrate, disseminated free gas and those areas that are void of any appreciable methane hydrate remains. The locations of apparent high-saturation methane hydrate are found along deep-seated faults and this saturation has a vertical orientation. Zones of apparent disseminated free gas and hydrate surround the high-saturation methane hydrate zones and are also seen extending to greater depths than methane hydrate.

REFERENCES

- Barnes, A.E. (2007) Redundant and useless seismic attributes, Society of Exploration Geophysicists, April, pp. 33-38.
- Beggs, M.; Wood, R.A.; Henrys, S.A.; Stagpoole, V.M. (2008), A roadmap for the commercial development of New Zealand's gas hydrate resources. Lower Hutt: GNS Science, GNS Science report 2008/06, Lower Hutt, New Zealand, p. 12.
- Boswell, R., Collett, T. (2006) The Gas Hydrates Resource Pyramid, Fire in the Ice, USDE, pp. 1-3.
- Brown, R. L., (1994), Image quality depends on your point of view: The Leading Edge, Vol. 13, pp. 669-673.
- Chopra and Marfurt (2005) Seismic attributes- a historical perspective, Geophysics, 70, 3S0-28S0.
- Chopra and Marfurt (2006) Seismic Attributes - a promising aid for geologic prediction, CSEG Recorder, Special Edition pp. 110-121.
- Chopra, S., and K. J. Marfurt, (2008), Emerging and future trends in seismic attributes: The Leading Edge, **27**, 298-318.
- Cordon et al. (2006) Seismic reflections of gas hydrate from perturbational forward modeling, Geophysics, vol. 71, pp. 165-171, doi: 10.1190/1.2356909.
- Collett, T.S., Ladd, J. (1999) Detection of gas hydrate with downhole logs and assessment of gas hydrate concentrations (saturations) and gas volumes on the Blake Ridge with electrical resistivity log data, Proc. Ocean Drill. Program Sci. Results Vol. 164, pp. 179-191.
- Collett, T.S. (2001) A review of well-log analysis techniques used to assess gas-hydrate-bearing reservoirs, Natural Gas Hydrates, Occurrence, Distribution and Detection, Geophysical Monograph Series, Vol. 124 American Geophysical Union (AGU), pp. 189-210.
- Demirbas, A. (2010) Methane hydrates as a potential energy resource: Part 1 – Importance, resource and recovery facilities, Energy Conversion and Management, Vol. 51, pp. 1547-1561.

- DeVore, J. L. and Farnum, N.R., (2005) APPLIED STATISTICS FOR ENGINEERS AND SCIENTISTS, 2ND EDITION, Cengage Learning, Independence, KY 41051, 632 p.
- Dickens, G. R., Castillo, M. M., and Walker, J. C. G., (1997), A blast of gas in the latest Paleocene: simulating first-order effects of massive dissociation of oceanic methane hydrate, *Geology*, v. 25, 259-262.
- Dunbar, J.A., Gunnell, A.G., Higley, P. (2010) Seafloor Resistivity Investigation of Methane Hydrate Distribution in Mississippi Canyon, Block 118, Gulf of Mexico, SAGEEP April, <http://www.eegs.org>.
- Edwards, NR (1997) On the resource evaluation of marine gas hydrate deposits using seafloor transient electric dipole-dipole methods, *Geophysics*, v. 62, no 1, pp. 63-74.
- Francisca, F, et al. (2005) Geophysical and geotechnical properties of near-sea-floor sediments in the northern Gulf of Mexico gas hydrate province, *Earth and Planet. Sci. Lett.* 237, pp. 924-939.
- Gei, D., Carcione, J.M., (2003) Acoustic properties of sediments saturated with gas hydrate, free gas and water, *Geophysical Prospecting*, Vol. 51, pp. 141-157.
- Ghosh, R. Sain, K, and Ojha, M., (2010) Estimating the amount of gas-hydrate using effective medium theory: a case study in the Blake Ridge, *Marine Geophysical Research*, v. 31, p. 29-37.
- Hardage, B.A., Roberts, H.H. (2006) Gas hydrate in the Gulf of Mexico: What and where is the seismic target?, *The Leading Edge*, May, pp. 566-571.
- Hato, M., Matsuoka, T., Inamori, T., Saeki, T. (2006) Detection of methane-hydrate-bearing zones using seismic attributes analysis, *The Leading Edge*, May, pp. 607-609.
- Helgerud, H. B., Waite, W. F., Kirby, S. H., and Nur, A., (2009), Elastic wave speeds and moduli in polycrystalline ice Ih, SI methane hydrate, and sII methane-ethane hydrate, *Journal of Geophysical Research*, v. 114, no. B02212, 11 p. doi:10.1029/2008JB006132.
- Hesthammer, J., Stefatos, A., Boulaenko, M., Fanavoll, S., Danielsen, J. (2010) CSEEM performance in light of well results, *The Leading Edge*, January, pp. 34-41.
- Hyndman, RD, Yuan, T, Moran, K (1999) The concentration of deep sea gas hydrates from downhole electrical resistivity logs and laboratory data, *Earth and Planet. Sci. Lett.* 172, pp. 167-177.

- Kvenvolden, K.A. and McMenamin, M.A. (1980), Hydrates of natural gas: A review of their geologic occurrence. U.S. Geological Survey Circular Vol. 825, pp. 11.
- Kvenvolden, K. A. (1993) Gas hydrates – geological perspective and global change, *Review of Geophysics* 31, pp. 173-187.
- Kumar, D., Sen, M., Bangs, N. (2006) Seismic characteristics of gas hydrates at Hydrate Ridge, offshore Oregon, *The Leading Edge* pp. 610-614, May.
- Lodolo, E., Camerlenghi, A., Madrussani, G., Tinivella, U., Rossi, G. (2002) Assessment of gas hydrate and free gas distribution on the South Shetland margin (Antarctica) based on multichannel seismic reflection data, *Journal Geophys. Int.*, Vol 148. pp. 103-119.
- Loke, M.H. (2010) Tutorial : 2-D and 3-D electrical imaging surveys, copyright (1996-2010).
- Luo, Y., S. al-Dossary, M. Marhoon, and M. Alfaraj, (2003) Generalized Hilbert transform and its application in geophysics: *The Leading Edge*, **22**, 198-202.
- Lutken, C et al. (2003) Interpretation of high resolution seismic data from a geologically complex continental margin, northern Gulf of Mexico, *GCAGS/GCSSEPM Transactions*, vol. 53.
- Max, et al. (1997) Methan Hydrate, A Special Clathrate: Its Attributes and Potential, *Naval Research Laboratory, NRL/MR/6101- - 97-7926*.
- McGee, T. et al. (2005) A Multidisciplinary Sea-floor Observatory in the Northern Gulf of Mexico: Results of Preliminary Studies, pp. 1-5.
- McGee, T. et al. (2008), Progress toward a sea-floor observatory at a carbonate/hydrate mound in the northern Gulf of Mexico, *US/EU-Baltic International Symposium*, IEEE: 978-1-4244-2267-8.
- McGee, T., (2009), Geologic structures associated with the carbonate/hydrate mound in Mississippi Canyon Block 118, Gulf of Mexico, *AGU fall meeting*, San Francisco, CA, December, 17, 2009.
- Ojha, M., Sain, K. (2007) Seismic velocities and quantification of gas-hydrates from AVA modeling in the western continental margin of India, *Mar Geophys Res*, Vol. 28, pp. 101-107, DOI 10.1007/s11001-007-9017-6.
- Paull, C., Matsumoto, R., Wallace, P.J. (1996) Introduction, *Proceeding of the Ocean Drilling Program, Initial Reports*, Vol. 164, pp. 5-11.

- Pearson, C.F., Halleck, P.M., McGuire, P. L., Hermes, R., Mathews, M. (1983) Natural Gas Hydrate Deposits: A Review of in Situ Properties, *J. Phys. Chem.*, Vol. 87, pp. 4180-4185.
- Priest, JA; Rees, EV; Clayton, CR (2009) Influence of gas hydrate morphology on the seismic velocities of sands, *J. Geophys. Research.* V. 114, doi: 10.1029/2009JB006284.
- Riedel, M et al. (2006) Estimates of in situ gas hydrate concentration from resistivity monitoring of gas hydrate bearing sediments during temperature equilibration, *Marine Geol.* vol. 227, 215-225.
- Rose, K., Boswell, R., Collett, T., (2011), Mount Elbert gas hydrate stratigraphic test all, Alaska North Slope: coring operations, core sedimentology, and lithostratigraphy, *Marine and Petroleum Geology*, v. 28, p. 311-331.
- Roy, A., and Apparao, A. (1971) Depth of Investigation in Direct Current Methods, *Geophysics*, v.36, no. 5, pp. 943-959.
- Ruppel, C., and Noserale, D. (2012) Gas Hydrates and Climate Warming – Sound Waves, USGS Issue No. 140, www.usgs.gov/blogs/deatures/usgs_science_pick/gas-hydrates-and-climate-warming.
- Saiki, T. et al. (2008) Delineation of methane hydrate concentrated zone using 3D seismic data in the eastern Nankai Trough, ICGH July 6-10.
- Sain, K., Ghosh, R., and Ojha, (2010), Rock physics modeling for assessing gas hydrate and free gas: a case study in the Cascadia accretionary prism, *Marine Geophysical Research*, v. 31, p. 109-119.
- Shipley, T et al. (1979) Seismic Evidence for widespread possible gas hydrate horizons on continental slopes and rises, *AAPG Bul.* v. 63, No. 12, pp. 2204-2213.
- Sleeper, K., Lowrie, A., Bosman, A., Macelloni, L. and Swann, C. T. (2006) Bathymetric mapping and high resolution seismic profiling by AUV in MC118 (Gulf of Mexico), *Proceedings of 38th Offshore Technology Conference*, 18133.
- Simonetti, A. et al., (2013) Spatial distribution of gas hydrates from high-resolution seismic and core data, Woolsey Mound, Northern Gulf of Mexico, *Marine and Petroleum Geology*, v. 44, pp. 21-33.
- Sloan, E.D. Jr. (1998) CLATHRATE HYDRATES OF NATURAL GASES, Marcel Dekker, New York, 705 p.

- Taner, M. T., F. Koehler, and R. E. Sheriff, (1979), Complex seismic trace analysis: Geophysics, 44, 1041-1063.
- Thakur, N. K., Rao, P. P., Vishwanath, N., Rajput, S. and Ashalatha, B., (2007), Tomographic approach for gas hydrate investigation in Kerala-Konkan region, India, Marine Geophysical Research, v. 28, p. 373-378.
- Weitemeyer, KA; Constable, SC; Key, KW; Behrens, JP (2006) First results from a marine controlled-source electromagnetic survey to detect gas hydrates offshore Oregon, Geophys. Res. Lett. v. 33 doi: 10.1029/2005GL024896.
- Zillmer, M., Flueh, E.R., Petersen J. (2005) Seismic investigation of a bottom simulating reflector and quantification of gas hydrate in the Black Sea, J of Int. Geophys, vol. 161, pp. 662-678, doi: 10.1111/j.1365-246X.2005.02635.x.